Sediment flows in South America supported by daily hydrologic-hydrodynamic modeling

Hugo de Oliveira Fagundes[1,1], Fernando Mainardi Fan[2,2], Rodrigo Cauduro Dias de Paiva[2,2], Vinícius Alencar Siqueira[2,2], Diogo Costa Buarque[3,3], Luísa Weizenmann Kornowski[1,1], Leonardo Laipelt[2,2], and Walter Collischonn[1,1]

[1]Institute of Hydraulic Research, Federal University of Rio Grande do Sul
[2]Institute of Hydraulic Research
[3]Department of Environmental Engineering

November 30, 2022

Abstract

Suspended sediments (SS) contribute to the maintenance of several ecosystems. However, intense soil erosion can lead to environmental, social, and economic impacts. South America (SA) has very high erosion and sediment transport rates. Here we present a detailed description of the spatio-temporal dynamics of natural SS flows in SA using the continental sediment model MGB-SED AS. We evaluate the model with daily in-situ data from 595 stations, information from regional studies and a global model. The model performance analysis showed that, in general, there was a better agreement between simulated and observed data than with the information found in regional studies and of the global model. The use of the hydrodynamic propagation method has allowed a better representation of sediment flows in rivers and floodplains. Based in the calibrated model results, SA delivers 1.00×109 t/year of SS to the oceans, in which the Amazon (4.36×108 t/year), Orinoco (1.37×108 t/year), La Plata (1.11×108 t/year) and Magdalena (3.26×107) rivers are the main suppliers. The floodplains play an essential role, retaining about 12% (2.40×108 t/year) of the SS loads reaching the rivers. In this study, datasets related to SS flows in SA were generated and can be used to support other large-scale researches or policymakers and stakeholders for adequate management of continental land use.

Sediment flows in South America supported by daily hydrologic-hydrodynamic modeling

H. O. Fagundes[1], F. M. Fan[1], R. C. D. Paiva[1], V. A. Siqueira[1], D. C. Buarque[2], L. W. Kornowski[1], L. Laipelt[1], W. Collischonn[1]

[1]Institute of Hydraulic Research, Federal University of Rio Grande do Sul, Porto Alegre, Rio Grande do Sul, Brazil

[2]Department of Environmental Engineering, Federal University of Espírito Santo, Vitória, Espírito Santo, Brazil

Corresponding author: Hugo Fagundes (h.o.fagundes@hotmail.com)

Key Points:

- First assessment of natural spatio-temporal sediment dynamics in South America from physically based model
- Floodplains anticipate the peak of suspended sediment discharge, and retain almost 12% of sediments
- South America exports 2.76 Mt/day of suspended sediments to the oceans; 44%, 14% and 11% come from Amazon, Orinoco and La Plata rivers

Abstract

Suspended sediments (SS) contribute to the maintenance of several ecosystems. However, intense soil erosion can lead to environmental, social, and economic impacts. South America (SA) has very high erosion and sediment transport rates. Here we present a detailed description of the spatio-temporal dynamics of natural SS flows in SA using the continental sediment model MGB-SED AS. We evaluate the model with daily in-situ data from 595 stations, information from regional studies and a global model. The model performance analysis showed that, in general, there was a better agreement between simulated and observed data than with the information found in regional studies and of the global model. The use of the hydrodynamic propagation method has allowed a better representation of sediment flows in rivers and floodplains. Based in the calibrated model results, SA delivers 1.00×10^9 t/year of SS to the oceans, in which the Amazon (4.36×10^8 t/year), Orinoco (1.37×10^8 t/year), La Plata (1.11×10^8 t/year) and Magdalena (3.26×10^7) rivers are the main suppliers. The floodplains play an essential role, retaining about 12% (2.40×10^8 t/year) of the SS loads reaching the rivers. In this study, datasets related to SS flows in SA were generated and can be used to support other large-scale researches or policymakers and stakeholders for adequate management of continental land use.

Key words: Continental-scale; Erosion; MUSLE; MGB

1 Introduction

Understanding erosion and sediment transport processes are relevant to comprehend geological changes and landscape evolution (Latrubesse et al., 2005; Syvitski and Milliman, 2007; Zhang et al., 2004), biogeochemical cycles (e.g., Beusen et al., 2005; Doetterl et al., 2012; Galy et al., 2015; Ito, 2007; Kuhn et al., 2009; Lal, 2003; Müller-Nedebock and Chaplot, 2015; Naipal et al., 2018; Tan et al., 2017; Van Oost et al., 2007; Willenbring and Von Blanckenburg, 2010), and impacts of human activities, such as land use/ land cover changes (e.g., Murphy, 2019; Oliveira et al., 2015; Panagos et al., 2017; Wang and Van Oost, 2019) and dams construction (e.g., Best, 2019; Cohen et al., 2014; Forsberg et al., 2017; García-Ruiz et al., 2015; Latrubesse et al., 2017, 2005; Restrepo et al., 2006; Syvitski et al., 2005). In the last 8,000 years, the conversion of natural vegetation into agriculture has resulted in an accumulated erosion of about 27,187± 9,030 Gt worldwide (Wang and Van Oost, 2019). Meanwhile, it is estimated that the impact of soil erosion on global GDP (Gross Domestic Product) is an annual loss of ~USS $8 billion, threatening the food security, leading to a global reduction in the production of 33.7 Gt/year and a consequent increase in water withdrawals of 48 billion m³/year (Sartori et al., 2019).

A large number of rivers with the largest sediment transports in the world (>100 Mt/year) are in South America (SA, Borrelli et al., 2017; Doetterl et al., 2012; Latrubesse et al., 2005; Mouyen et al., 2018; Naipal et al., 2018; Syvitski et al., 2014, 2005; Wuepper et al., 2019). The Amazon River is at the top of the list (Latrubesse et al., 2005), transporting about 555 Mt/year at Óbidos (Filizola and Guyot, 2009).. Borrelli et al. (2017) observed high erosion rates (>10 t/ha.year) in SA in 2012, which increasing tendency compared to the 2001 year. This severe erosion has contributed to generate, for example, a reduction in food production of 8,170 Mt/year in Brazil (Sartori et al., 2019). Researches have shown that climate changes will impact the land use/ land cover (Almagro et al., 2017; Brêda et al., 2020; Cohen et al., 2014) and that the implementation of many dams will affect the connectivity of water flows even more, sediments, nutrients, and aquatic organisms (Forsberg et al., 2017; Grill et al., 2019; Latrubesse et al., 2017).

In the last decades, great efforts have been dedicated to understanding and quantifying sediment loads around the world. The use of in-situ measured data is one of the main tools used to estimate the transport in rivers (e.g., Best, 2019; Dearing and Jones, 2003; Latrubesse et al., 2005; Mouyen et al., 2018; Murphy, 2019; Niu et al., 2014; Restrepo et al., 2006) or watershed erosion rates (e.g., García-Ruiz et al., 2015). However, there is a lack of measurements of sediments in both intra-basin (e.g., García-Ruiz et al., 2015; Kettner et al., 2010; Lima et al., 2005) and near the Oceans, where less than 10% of rivers have monitoring of sediment delivery to coastal zones (Syvitski et al. 2005). Notably, in the era of big data and big science, there are still a lack of hydrological, sediment, and nutrient data available in the world's large rivers (Best, 2019). The lack of data represents a major barrier to develop analyses for large scales (continental or global) that require long time series (Dearing and Jones, 2003).

Computational sediment models have helped to fill this gap of sediment information. For the global scale, several applications have been carried out with Universal Soil Loss Equation (USLE, e.g., Xiong et al., 2019, 2018) – developed by Wischmeier and Smith (1978) – and its revised version RUSLE (e.g., Borrelli et al., 2017; Naipal et al., 2018, 2015; Sartori et al., 2019; Wuepper et al., 2019; Yang et al., 2003). According to Alewell et al. (2019), USLE and RUSLE are the most used models around the world. However, approaches that used these models were focused only on soil loss spatial representation, with long-term average estimates, which do not allow to understand the dynamic processes that involve sediment flows, such as the loads transported by the rivers. In this perspective, global sediment transport models were developed to estimate the impact of human activities on sediment delivery to the oceans (Syvitski et al. 2005), characterize rivers in terms of transported sediment loads (Cohen et al., 2013; Pelletier, 2012), and assess regional trends and variabilities (Cohen et al. 2014). The global models are generally empirically-based and have few input parameters, which facilitate applications on these scales. Nevertheless, these models have been poorly validated, they were focused on estimating long-term annual averages (e.g., Cohen et al. 2013; Pelletier 2012; Syvitski and Milliman 2007), and are based on simplified methodologies to estimate hydrological variables and sediment routing.

Despite the barriers encountered in the model applications on a global scale, few papers are found in the literature regarding continental scales. Panagos et al. (2015) used the RUSLE2015 model to estimate erosion rates for the reference year 2010 across Europe, with a spatial resolution of 100 m. Campagnoli (2006) used an approach (not fully described) focused on geological and geomorphological aspects to generate an annual sediment yield map of South America. However, as mentioned in the previous paragraph, these approaches are not capable to fully describe dynamic sediment processes.

The global model WBMsed used by Cohen et al. (2014) uses the simplified Muskingum-Cunge routing method (Wisser et al., 2010). The global models of Pelletier (2012) and Syvitski and Milliman (2007) do not explicitly consider the rivers flow routing. Studies performed in several South America regions have shown that simplified methods are sometimes not suitable to represent backwater and floodplain effects, which can be driving factors in flow routing in large basins (e.g., Angarita et al., 2018; Bravo et al., 2012; Paiva et al., 2013, 2011; Pontes et al., 2017; Siqueira et al., 2018; Zhao et al., 2017).

On the other hand, when we compare the sediment modeling studies with hydrological-hydrodynamic modeling studies, one can see that significant advances have been made in the later for global and continental scales. For example, studies made by Hanasaki et al. (2006), Hanasaki et al., (2008a, 2008b) and Hanasaki et al. (2018) showed global scale simulations with many capabilities to represent the global hydrological cycle and the human interference on it, such as water abstractions and rivers impoundments. The van Beek et al. (2011) study used the global PCR-GLOBWB model to evaluate water availability and water stress on a monthly scale for the whole globe. Meanwhile, the study by Beck et al. (2017) shows how extensive global hydrological models development research is, while evaluating the runoff estimates generated across the globe by six global models in addition to four land surface models. Other examples, with a greater focus on the fluvial hydrodynamic representation, are the studies of Yamazaki et al. (2011) and Yamazaki et al. (2013), which showed global model applications for flooding applications, including the impact of floodplains. Also, most of the models developed in recent years simulate processes on a daily scale (Bierkens, 2015). Many of them have the concept of "hyperresolution models" as their motivation, which aims to simulate processes on a global scale, but whose results are useful on a local scale (e.g., Bates et al., 2018; Wada et al., 2014; Wood et al., 2011).

On the continental scale, progress in the development of hydrological and hydrodynamic models also stand out, with dam representation (Shin et al., 2019) and improvements in fluvial hydrodynamics (Siqueira et al., 2018). The National Water Model (NWM, http://water.noaa.gov/about/nwm) developed in 2016 by National Oceanic and Atmospheric Administration (NOAA), which has been conducting simulations and streamflow forecasts for the United States, can be mentioned as an example. The study of Siqueira et al. (2018) applied for the first time a continental-scale fully coupled hydrological-hydrodynamic model for the whole South America. The Siqueira et al. (2018) results showed that limitations on flow estimation by state-of-the-art global models could be reduced using better calibrated continental models, which represent relevant processes (e.g., hydrodynamics) for the area of interest, and which are built on previous experience of regional-scale studies.

While these cited examples of hydrologic and hydrodynamic modeling with continental and global scales have increasingly appeared in the literature, including the goal of attaining "hyperresolution" models, no study has been found in the literature to estimate continental-scale sediment transport having hydrologic-hydrodynamic processes integrated. There is then a gap between the advances in large scale hydrologic and hydrodynamic modeling and the advances in sediment modeling at continental and global scales.

Bridging the gaps between recent advances in hydrologic and hydrodynamic modeling at continental scales and sediment modeling provide some opportunities: (i) obtain models that allow the comprehension and comparison of spatial and temporal dynamics explicitly, and that still represent important processes such as backwater effects in the rivers and the lateral flow exchange of water and sediments with floodplains (e.g., Buarque, 2015; Cohen et al., 2013; Grill et al., 2019; Paiva et al., 2013, 2011; Pontes et al., 2017; Rudorff et al., 2018); (ii) obtain continental or global scale models that are well-validated to provide locally relevant information at multiple time scales and suitable for policymakers and stakeholders (Bierkens, 2015; Fleischmann et al., 2019b; Siqueira et al., 2018); (iii) acquire continental sediment discharges information not only in the outlets of large rivers but also intra-basin. These items, therefore, become the interest of this study, which has South America as a subject of study, and aims to answer the following specific questions from modeling results: what is the accuracy of the proposed continental sediment model? What are the potential transported loads by the rivers in the continent? What are the spatial and temporal dynamics of sediment flows over South America? What is the impact of fluvial hydrodynamics on sediment transport and deposition? In which regions do suspended sediments deposit the most? To answer these questions, we have developed and evaluated the performance of sediment erosion and transport model for the entire South American domain.

2 Overview of Sediment-Related Processes in South America

South America (SA) transports ~20% of the sediments reaching the oceans (Syvitski et al., 2005), and the Amazon and Magdalena rivers (Figure 1-a) are among the world's largest sediment delivers (Mouyen et al., 2018). SA has the second-highest potential erosion rate on the planet and the highest increase in the last century (Wuepper et al., 2019). This increase also attributes to SA the highest rate of particulate organic carbon erosion. (Naipal et al., 2018). Among the causes of these changes are agricultural expansion and deforestation (Borrelli et al., 2017), which have been increasing, causing concerns in the Amazon basin (Aguiar et al., 2016; Aragão, 2012).

Most of the SA is located in tropical regions that have little interannual variability between sunrise and sunset and receive high solar incidence. The Intertropical Convergence Zone (ITCZ) directly influences the establishment of dry and rainy seasons; El Niño events; and the South Atlantic Convergence Zone (SACZ), which causes heavy precipitations in the summer. Annual precipitation variability is strong, with desert regions in Chile and rainfall reaching approximately 10,000 mm in Colombia (Latrubesse et al., 2005).

Rivers that drain the Andean region transport the highest sediment load on the continent. According to Restrepo et al. (2006), the Magdalena River is the one with the highest average sediment yield (690 t/km^2.year). More than 90% of the suspended sediment (SS) load of the Amazon Basin comes from the Andes (Latrubesse et al., 2005). Filizola and Guyot (2011), using in-situ measured data, indicate that the Madeira River (Figure 1-a) contributes almost 50% to the Amazon River solid discharge, in which the Beni and Mamoré rivers represent about 72% and 28%, respectively, of the Madeira transport. (Guyot et al., 1999). The Ucayali River drains the Peruvian Andean part and is also one of the SA rivers with the highest SS load (Latrubesse et al., 2005). Rivers originating in the South Andean regions also carry high SS loads, such as the Bermejo River, which provides about 90% (Amsler and Drago, 2009) and the Pilcomayo river about 140 Mt/year of the total load carried by the Paraná River (Latrubesse et al., 2005). Lima et al. (2005) observed that smaller rivers like Parnaíba, Paraíba do Sul and Doce (Figure 1-a), although they do not have the highest sediment yield rates ($t/year.km^2$), they have high values of suspended sediment concentrations (SSC) (Lima et al. 2005). According to Latrubesse et al. (2017), Cratonic rivers such as the Negro, Tapajós and Xingu present low SS loads. At the same time, the Araguaia (Latrubesse et al., 2005), Tocantins (Latrubesse et al., 2005), Paraná (Amsler and Prendes, 2000) and Orinoco (Meade et al., 1990) rivers have intermediate values of SS yield.

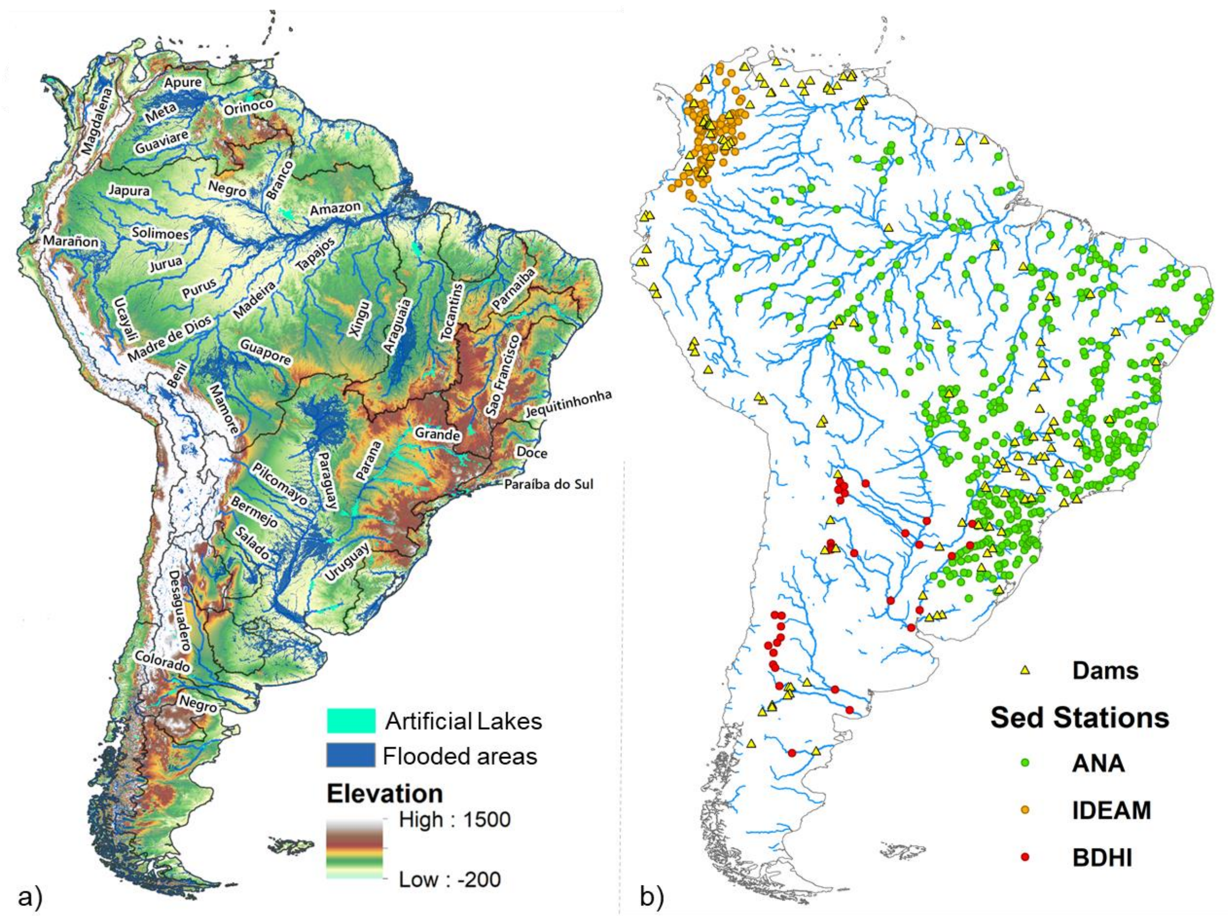

Figure 1: South America showing: a) major hydrological regions according to FAO and *Agência Nacional de Águas do Brasil* (ANA) classifications, relief map based on the Bare-Earth SRTM (O'Loughlin et al., 2016), including main rivers, flooded areas (Fluet-Chouinard et al., 2015) and artificial lakes (Lehner et al., 2011); and b) existent dams from GRanD v1.3 product (>0.1 km³ Lehner et al., 2011 - http://globaldamwatch.org) and from ANA (> 30MW), and sediment stations from ANA, *Base de Datos Hidrológica Integrada da Argentina* (BDHI) and *Instituto de Hidrologia, Meteorologia e Estudos Ambientais da Colômbia* (IDEAM)

The floodplains have an important ecosystem function and storage part of the sediment loads transported in the SA. In the Amazon basin, about 50% of the sediments leaving the Andes are deposited in the floodplains (Guyot et al., 1989), and in the Pilcomayo basin (Figure 1-a), this value is even greater (Latrubesse et al., 2005). Sediment trap also occurs through anthropic factors, such as the presence of impoundments (Figure 1-a), which cause disturbances in river systems, decreasing the sediment load and affecting the geomorphology and the downstream floodplain productivity (Almeida et al., 2015; Grill et al., 2019; Latrubesse et al., 2017, 2005; Restrepo et al., 2006). The highest sediment trap rates (80% - 100%) in SA dams are found in the São Francisco, Tocantins, Orinoco, La Plata and Negro (Argentina) rivers (Syvitski et al. 2005). By using surface samples in the Madeira River, Rivera et al. (2019) estimated a depletion of 30% in the fine suspended sediment concentration after the construction of Jirau and Santo Antonio dams. According to Latrubesse et al. (2017), the existing dams (as well as dams under construction and planned ones) have potential to impact mainly Madeira, Upper Solimões and Tapajós basins.

Despite the knowledge provided by previous studies, some things are not yet fully understood: the effect of fluvial hydrodynamics on sediment flows; thoroughly and accurately, the spatiotemporal patterns of denudation rates, concentration (SSC), solid discharge (QSS) and suspended sediment deposition; the driving factors in the relation between SSC/QSS and water discharge; the annual sediment balance of the SA and its main rivers; the potential consequences of climate changes on the patterns of these variables; the impact of dams on rivers and those with the greatest potential to be affected; the relevance of landslides in the sediments transport of each river; and the relative contribution of the anthropic activities, such as mining, to the sediment flows.

3 South America Sediment Model

To elucidate the South America sediment flows, we used the MGB-SED sediment model (Buarque, 2015; Fagundes et al., 2019, 2020; Föeger, 2019) coupled to hydrologic-hydrodynamic model MGB AS, presented by Siqueira et al. (2018). This modeling configuration was chosen for three main reasons: (i) it is the first fully coupled hydrologic-hydrodynamic model, developed for regional scales, applied for South America's continental domain; (ii) the model has a high temporal resolution (daily outputs) and was validated in most of SA using in-situ and other sources of hydrological data, showing that hydrological variables were well represented; and (iii) the performance of sediment models can be strongly affected by the performance of hydrological models (Cohen et al., 2013; Shen et al., 2012), and the MGB AS has a better performance compared to the global models evaluated by Siqueira et al. (2018).

3.1 MGB AS Hydrologic-Hydrodynamic Model

The *Modelo Hidrológico de Grandes Bacias* (MGB) was initially developed by Collischonn et al. (2007) and further improved to address different questions (e.g., Fleischmann et al., 2019, 2018; Paiva et al., 2011; Pontes et al., 2017; Siqueira et al., 2018). It is a conceptual model, semi-distributed, and has spatial discretization defined by unit catchments (Pontes et al., 2017), each with its own river stretch and floodplain. Precipitation is the main driver of the model (it does not consider snow or ice melting), from which hydrological processes are simulated, such as: canopy interception, soil infiltration, evapotranspiration, and routing of surface, subsurface and groundwater flows. Each unit catchment can have several Hydrological Response Unit (HRU), which is a combination of soil type and soil cover (Kouwen et al., 1993), where water and energy are computed. Surface, subsurface, and groundwater volumes are stored in simple linear reservoirs and further routed to the stream network.

In the following, a brief description of the methodology used by Siqueira et al. (2018) is presented. We use the same MGB AS settings and structure, as well as the input data used by the authors. They found agreement between the simulated and observed flows that resulted in a Nash-Sutcliffe efficiency coefficient (NSE) > 0.6 in more than 55% of the analysed stations.

Flow routing in the drainage network is performed using the local inertial method (Bates et al., 2010; Pontes et al., 2017). The continuity equation is used to estimate the stored volume, flooded area, and streamflow and floodplain water level. Floodplains are represented as storage areas that compute evaporation in open waters, assuming that water level is constant for the whole unit catchment. Floodplains water infiltration for unsaturated soils are still considered (as described by Fleischmann et al., 2018), specifically for the Pantanal wetlands.

MGB AS model also allows using the Muskingum-Cunge (MC) method to routing flows. This method takes a time interval that is subdivided into smaller intervals and also split the total river reach length into sub-reaches to route the flows. The MC method enables the representation of flood wave translation and smoothing, that routes at a velocity c (celerity) higher than average streamflow velocity in a specific time interval and river reach. Among the method advantages are the more straightforward implementation, lower computational efforts, and numeric stability. As for disadvantages, there are the non-representation of backwater effects and lateral exchanges between river and floodplain, which may play an important role in large basins (Getirana and Paiva, 2013).

MGB-SA was built using the 15 arcsec HydroSHEDS flow direction map (Lehner et al., 2008) and a minimum drainage area threshold of 1,000km², and basins were discretized into unit-catchments with fixed river lengths equal to 15 km (Siqueira et al., 2018). The Digital Elevation Model (DEM) Bare-Earth SRTM v.1 (O'Loughlin et al., 2016) was used to compute the Height Above Nearest Drainage (HAND), from which the floodplain topography was estimated at a sub-grid level. River hydraulic geometry was set using the global data set of Andreadis et al. (2013), enhanced using information from regional studies (Beighley and Gummadi, 2011; Paiva et al., 2013, 2011; Pontes, 2016).

Precipitation data from global Multi-Source Weighted Ensemble Precipitation – MSWEP v1.1 (Beck et al., 2017) were used. The climatic variables used to estimate evapotranspiration were temperature, atmospheric pressure, income shortwave solar radiation, relative humidity, and wind speed obtained from Climate Research Unit (CRU) Global Climate v.2 (New et al., 2002). They are long-term monthly averages (1961-1990) and have 10' spatial resolution. South America HRUs map from Fan et al. (2015) was used to represent soil type (shallow and deep) and soil cover.

For more details about approaches, equations, and data, a full description can be found in Siqueira et al. (2018).

3.2 MGB-SED sediment model

The *Modelo de Sedimentos de Grandes Bacias* (MGB-SED) was introduced by Buarque (2015) and improved in other studies (e.g., Fagundes et al., 2020; Fagundes et al., 2019; Föeger, 2019). The MGB-SED has three modules (basin, river and floodplain) and enables the simulation of rill and interrill erosion processes in hillsides, bed river erosion and deposition, sediment transport through the river network, and deposition of suspended sediment in the floodplains.

The sediment volumes from hillsides to river reaches in each unit catchment is the primary information estimated by the model using the Modified Universal Soil Loss Equation (MUSLE) (MUSLE, Williams, 1975) :

$$Sed = \alpha.(Q_{sur} * q_{peak} * A)^{\beta}.K.C.P.LS_{2D} \quad (1)$$

where Sed[t/day] is the sediment yield, Q_{sur}[mm/day] is the specific runoff volume, q_{peak}[m³/s] is the peak runoff rate, A[ha] is the unit catchment area, K[0.013.t.m².h./m³.t.cm] is the soil erodibility factor, C[-] is the cover and management practices factor, P[-] is the conservation practices factor, LS_{2D}[-] is a bidimensional topographic factor; and α and β are the fit coefficients of the equation (which are calibrated afterward), whose values originally estimated by Williams (1975) were 11.8 and 0.56, respectively.

Q_{sur} and q_{peak} values are estimated by the coupled hydrologic model (MGB AS in this study). P factor is estimated from the knowledge of soil management and conservation practices but has been adopted as 1 in most large scale applications (e.g., Benavidez et al. 2018; Borrelli et al. 2017; Naipal et al. 2015; Phinzi and Ngetar 2019). C factor is usually calculated from field experiments but has been usually adopted from literature for each soil cover, as presented by Benavidez et al. (2018) and Phinzi and Ngetar (2019). MGB-SED model computes K factor from Williams (1995) equation, in which considers the soil texture (sand, silt and clay percentages) and amount of soil organic carbon. LS_{2D} factor is estimated by the model using a DEM (Buarque, 2015) and more details about the LS_{2D} estimates can be verified in the supplementary material S1.

The approach used by MGB-SED to estimate sediment yield using MUSLE equation is the same used in other models, as SWAT (Arnold et al., 1998), CREAMS (Knisel, 1980), PERFECT (Littleboy et al., 1992) and SWIM (Krysanova et al., 1998). We are aware of the known limitations of this approach, as it does not explicitly consider all erosive processes such as those related to mass movements. Some authors like Tan et al. (2018) have already improved the estimates of a sediment model by including the representation of shallow landslides. However, as an initial approach and because it has already presented itself sufficiently in other large-scale modeling applications (e.g., Buarque, 2015), we use it, and we are aware of the limitations it imposes on the analysis of the results.

After computing sediment yield by MUSLE, the estimated volume is divided into three classes of particle sizes (silt, clay and sand), according to the percentage of these classes in the soil. Three linear reservoirs (one for each class) are used for the sediment routing from the hillsides to the drainage network. Each soil particle size is then routed from upstream to downstream using the following approaches: (i) for the fine loads (silt and clay), the unidimensional transport equation without the diffusion term is used, and the sediments are transported in suspension, without deposition in the channel; (ii) for sand, considered as bed load, the Exner sediment continuity equation is used together with the Yang transport capacity equation (Yang, 1973) to quantify the transport in the channel, the erosion or deposition in the bed. It is worth mentioning that in this study only the transport of suspended sediment load (silt+clay) is evaluated.

In the floodplains, a zero longitudinal velocity is assumed, and only river-floodplain exchanges are possible. The perfect mixing in the floodplains is also assumed, which implies constant concentrations of silt and clay in the vertical profile. Floodplains work as storage areas, where fine particles can be deposited but cannot be resuspended. Sediment deposition in the floodplains is estimated considering the fall velocity proposed by Wu and Wang (2006). Sediments that do not deposit flow back to the main channel.

More details about model equations can be found in the supplementary material S1. A summary of the coupling between the two models that resulted in the MGB-SED AS, main input data, processes, and outputs are shown in Figure 2.

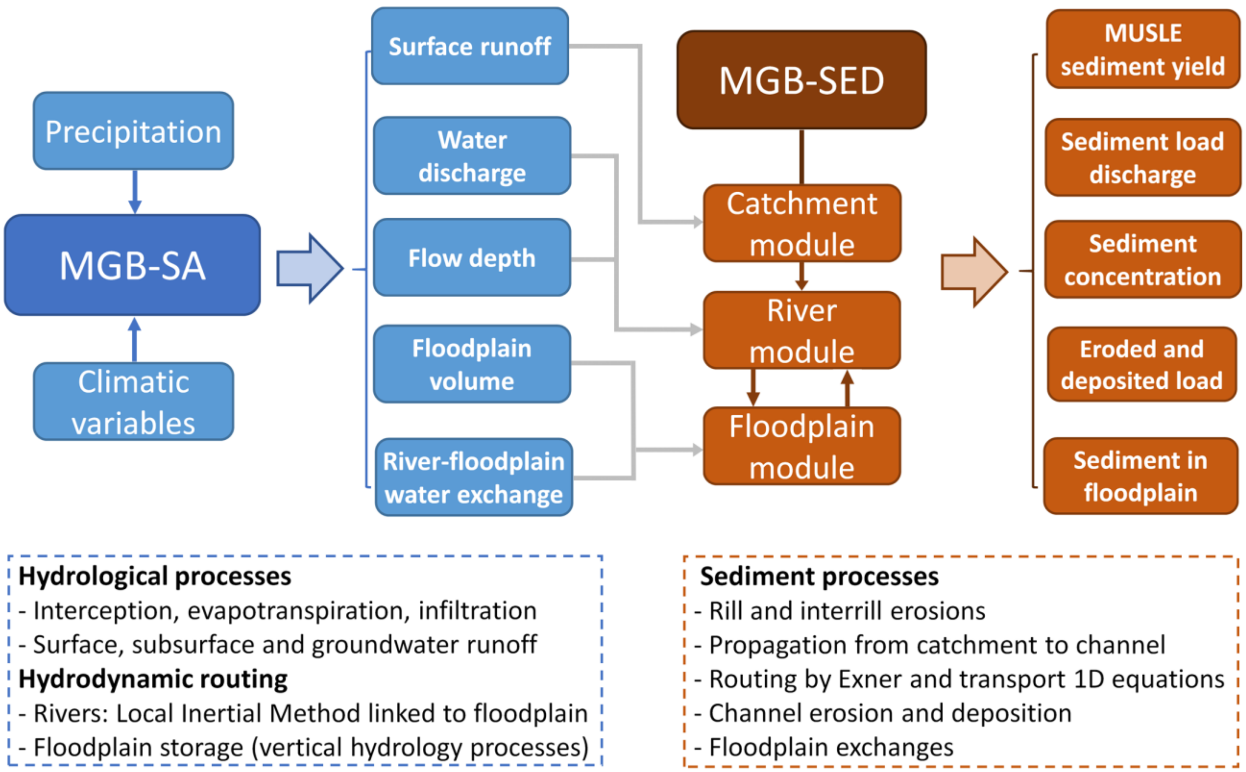

Figure 2: MGB-SED AS scheme. The blue (brown) part is related to the hydrological (sediment) model, its structure, main input data, processes, and main outputs.

3.3 Simulation Input Datasets

MGB-SED model requires topographic, soil type, texture and cover, and surface runoff to estimate daily sediments using the MUSLE equation. To compute K factor (Figure 3-a), we use percentages of silt, clay, sand and organic carbon for each soil type from the Food and Agriculture Organization (FAO) of the United Nations (FAO/UNESCO, 1974). LS_{2D} factor (Figure 3-b) was estimated using Bare-Earth SRTM v.1 DEM (O'Loughlin et al., 2016). We use each land cover identified in URH South America map (Fan et al., 2015) to compute C factor (Figure 3-c) based on previous studies (Benavidez et al., 2018; Buarque, 2015; Fagundes et al., 2019). It is worth mentioning that C values for the forest were not the same throughout SA, due to the heterogeneity of forest coverings (see Figure S1 - Supporting Information). P factor was adopted equal to 1, since in that scale there is no detailed information about soil conservation practices.

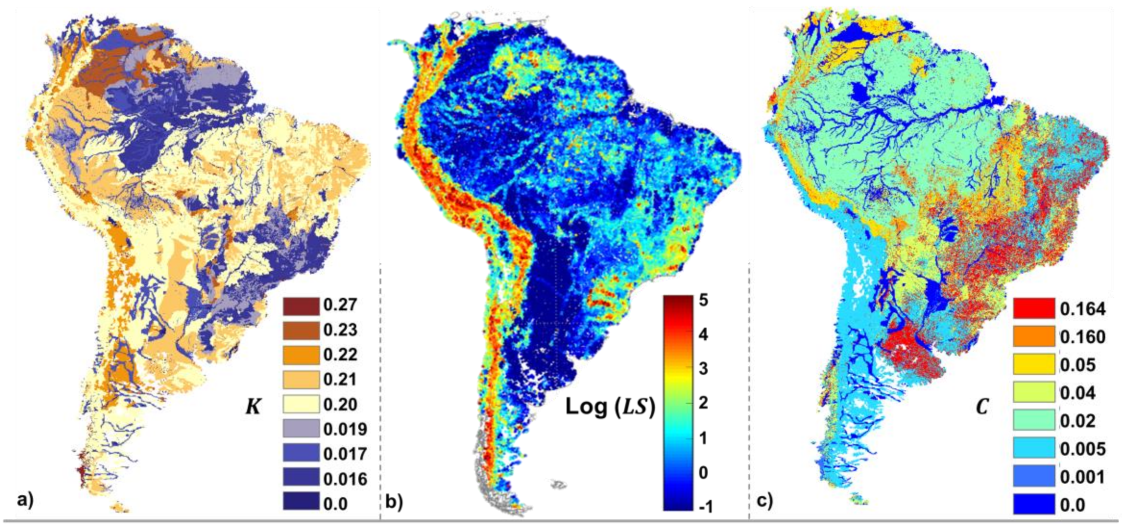

Figure 3: MUSLE parameters adopted for South America: a) K [0.013.t.m².h./m³.t.cm] factor; b) Log (LS_{2D}) [-] factor; and c) C [-] factor.

As mentioned before, the daily runoff was estimated by MGB AS and it was also used to compute q_{peak}. From this data and other simulated hydrological variables (e.g., river discharge and water level, and floodplains stored volumes), it was possible to compute soil loss and sediment transport using the same spatial discretization of MGB AS. We have chosen to change the values of the adjustable parameters α and β, as it has been done in several works (see the review presented by Sadeghi et al. (2014)), including previous applications with the MGB-SED model (e.g., Fagundes et al., 2019).

3.4 Experimental Design

3.4.1 Model Calibration and Evaluation

The base period for the analysis and performed simulations using the MGB-SED AS model was 1990-2009, in which the first two years were used to warm up the model. Initially, we performed a mass balance to check if the model was generating numerical errors, adding or removing mass in the simulation.

In order to know the natural (without impoundments) simulated sediment loads transported by the rivers, it was necessary to evaluate the performance of the MGB-SED AS model. For that, we used suspended sediment discharge (QSS) of the 595 in-situ stations (Figure 1-b) in Brazil - ANA (450), Colombia - IDEAM (109) and Argentina – BDHI (36). Suspended sediment is measured using cross-sectional mean sediment mass concentration, using the ISO 4363 (2002) protocol as reference. There are differences depending on river width and discharge. The main difference is found for IDEAM information, in which daily surface samples are taken and correlated against cross-sectional mean sediment mass concentration (IDEAM, 2007). ANA, BDHI, and IDEAM provide information of suspended sediment quarterly, monthly, and daily, respectively. Moreover, as samples are often not collected during flood events (in cases of ANA and BDHI), time series may be biased due to the predominance of data from the dry period. To address this continental sediment modeling we assume that uncertainties related to different sampling methods are not enough to prevent a comparison against modeling results.

To increase confidence and consistency, we used only databases for which samples are taken from the whole cross-section, or data are derived from the latter. Both observed data and simulations do not consider the organic solids. Free sediment data from other countries were not found. To better explore the data, stations having at least 4 measurements in the period of 1992-2009 and drainage area above 1,000 km² were selected.

In the calibration (2002-2009), 77 stations were used, with drainage areas ranging from 3,045 to 4,700,503 km². The calibration stations were selected as follows: i) we always choose stations with the largest drainage area for each monitored sub-basin; ii) in case stations were located downstream of one (or more) reservoir (Figure 1), the one upstream with the largest drainage area would be used; iii) when there was just one station in a sub-basin, it was used to calibrate the model.

The calibration was performed in two stages: an automatic calibration followed by a manual calibration. Automatic calibration was performed using the MOCOM-UA optimization algorithm (Yapo et al., 1998) following the recommendations proposed by Fagundes et al., (2019). The algorithm MOCOM-UA requires setting some parameters and initial conditions. We used a population of 100 individuals; three objective functions - Nash-Sutcliffe efficiency (NSE, Nash-Sutcliffe, 1970) efficiency coefficient, $BIAS$, and error in the slope of the duration curve between 10% and 50% ($DCPerm$, Kollat et al., 2012); maximum of 500 iterations; and three calibration parameters: α and β (Equation 1) and Ɣ (Equation 2). These parameters were adjusted to each model sub-basin.

$$ƫ = Ɣ.TKS \quad (2)$$

TKS (s) is the parameter which indicates the delay time of the surface linear reservoir output (Collischonn et al., 2007); ƫ (s) indicates the travel time of the sediments to the drainage network (see Text S1 in the support information S1); Ɣ [-] is the adjustment factor between the two aforementioned parameters. It means that surface runoff and sediment load transport can have different travel times between the hillsides and channels, and Ɣ can increase or decrease this difference. This approach is used to better represent the sediment processes, and overcome some limitations due to the use a large-scale sediment model. The range of values used for the calibration parameters α, β and Ɣ was, respectively, 0.01-25.0, 0.1-0.5 and 0.1-5.0.

For the basins where we have not data, a simple transfer of parameters from the calibrated sub-basins was made. The transfer process was based on the physical and climatic characteristics of the region.

For the validation (1992-2009), the same criteria of the calibration stage were used, resulting in the selection of 56 sediment stations. A global evaluation of the model performance was also carried out using the 595 stations. It was a conservative decision, which includes the model evaluation for the 1992-2009 period with the stations used (77) and those not used (518) in the calibration process. In addition to the metrics already mentioned, the model performance was evaluated using Pearson's correlation coefficient (r), Kling-Gupta (KGE) efficiency coefficient and relative value of Root Mean Square Error ($RMSE$).

MGB-SED AS results were compared to estimates from several regional studies (see Table S1 - Supporting Information). The comparison was performed using data of long-term average annual QSS from 80 sites exceeding a drainage area of 5,000 km² (see Table S1 and Figure S2, Supporting Information). The agreement between QSS simulated and those of regional studies was evaluated from the relative difference between the annual values (Equation 3).

$$Diff(\%) = 100x\frac{QSS\ MGB\text{-}SED\ AS - QSS\ reg.studies}{QSS\ reg.studies} \tag{3}$$

Positive (negative) $Diff$ values mean that MGB-SED AS model calculated values higher (lower) than those from regional studies used in the comparison.

QSS simulated was also compared to the outputs of the global sediment model WBMsed (Cohen et al., 2014). This model was selected because it is the only one with data freely available for society. It is a grid model with 6 arc-min (~11km) spatial resolution and uses the Muskingum-Cunge method to route daily water streamflows (Wisser et al., 2010). To estimate the QSS, firstly, the model computes the long-term average values using global empirical equation BQART (Syvitski and Milliman, 2007) and then it uses the Psi model (Morehead et al., 2003) to compute daily data. In the version presented by Cohen et al. (2014) the floodplains were represented as temporary (final) storage areas for water (sediment). It means that the flows reach the floodplains when the bankfull discharge is exceeded, and water can return to the river when discharge is below bankfull.

The $Diff(\%)$ was also used for the comparisons between MGB-SED AS and WBMsed outputs in 51 sites (see Table S2 and Figure S2, Supporting Information). The WBMsed grid cells identification was performed manually, and the selected sites are the same as the in-situ stations used for the comparisons against regional studies, which enable contrasts between scales and studies. Long-term average QSS were computed with both models in the period 1993-2009. The WBMsed outputs can be obtained at https://sdml.ua.edu/datasets-2/datasets/.

3.4.2 Analysis of Sediment Flows in South America

A study of QSS patterns was conducted using time series, from the calibrated model. QSS were simulated using the inertial and Muskingum-Cunge routing methods to assess the impact of fluvial hydrodynamics and floodplains on sediment transport and deposition. We also evaluate the effect of calibration and hydrodynamic routing on sediment delivery to the Oceans. For this purpose, we compared the estimated loads from a simulation considering hydrodynamic routing without calibration (i.e., setting the values 11.8 and 0.56 for parameters α and β, respectively) versus simulations using the inertial and Muskingum-Cunge methods to estimated loads considering the calibrated model.

To understand the spatial dynamics of the sediment flows in the SA, long-term averages of SSC, denudation rate, deposition of suspended sediment in the floodplains, and water discharge were calculated. We identified the major floodplains where the highest deposition rates occur, but the results were only presented for those basins where the model was calibrated, i.e., where there was no transfer of parameters, as in the case of the Orinoco River basin. We also computed the annual sediment balance at the outlets of the large rivers and for the whole SA.

4 Results and Discussions

4.1 Model Validation

4.1.1 Simulated data vs. in-situ observations

The mass balance analysis (Table S3, Supporting Information) showed that the MGB-SED AS model remained stable throughout the simulation. Numerical errors were of the 10^{-2}% order, mostly coming from variables truncation in the operations.

The simulated QSS was compared against observed daily values, and the performance of the model was evaluated in Figure 4 in terms of r, $BIAS$ and NSE. Other metrics are shown in Figure S3 of the Supporting Information. The better performance is found in the Amazon, Tocantins, São Francisco and Doce basins.

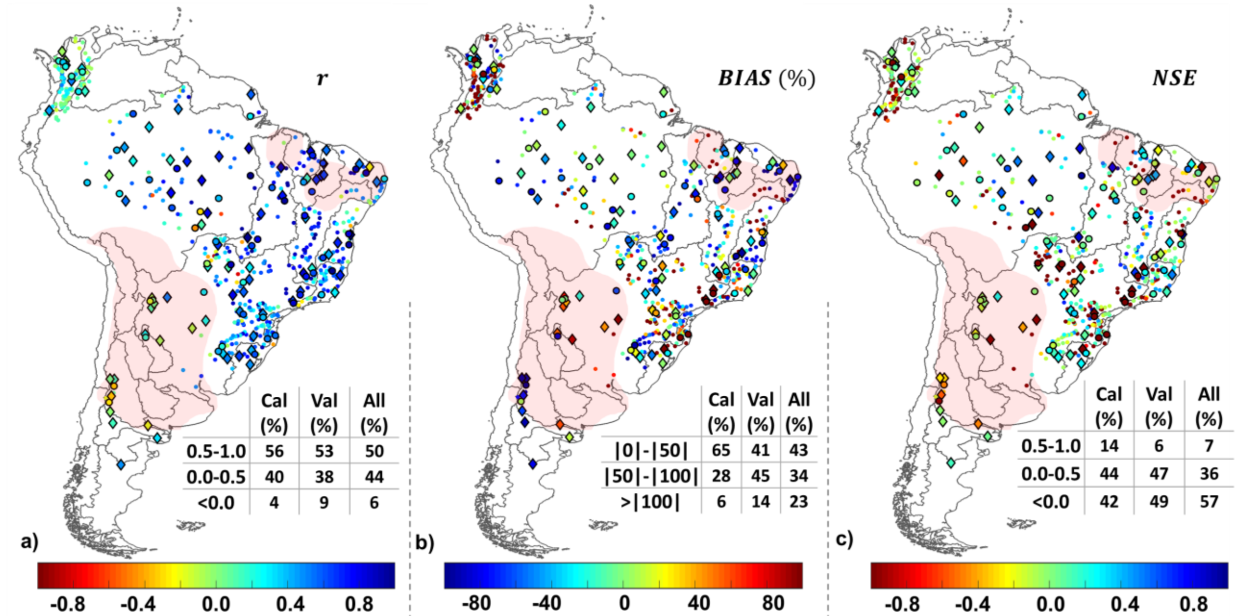

Figure 4: MGB-SED AS performance over South America in terms of suspended sediment discharge: a) correlation (r); b) $BIAS$ (%); and c) Nash-Sutcliffe efficiency (NSE). Diamonds and bigger dots refer to stations used in calibrating (Cal) and validating (Val) steps, respectively. Small dots refer to other station used to evaluate the model. Tables summarize the percentage of sediment stations in each performance class and corresponding step. Marked regions represent those with poor hydrological-hydrodynamic performance (see Siqueira et al., 2018).

Figure 4-a indicated agreement between model estimates and observed data in terms of correlation, in which 56% and 53% of the stations had values higher than 0.5 in the calibration (Cal) and validation (Val) steps, respectively. In terms of $BIAS$, 94% (Cal) and 86% (Val) of the stations had values between -100% and 100% (Figure 4-b). For NSE, 58% and 53% of the stations had positive values (Figure 4-c). Some underestimates (negative $BIAS$) can be due to high rates of sands in suspension, as pointed by Santini et al. (2019) for the upper areas of Amazon basin. According to the authors, these rates tend to decrease from upstream to downstream. Detailed views of regions having high density of stations are shown in Figures S4, S5 and S6 (Supporting Information).

In the evaluation using all stations (All), Figure 4 shows that MGB-SED AS model had a lower performance in comparison to calibration. We observed a better model performance to simulate QSS for stations used in the calibration, and worse model performance (r, NSE<0.0 and $BIAS$>|100) was noticed especially in three situations. The first one is related to the regions where the hydrological model performed poorly (Figure 4), characterized by arid or semi-arid climate; regions where snow melting plays an important role for the runoff generation; and regions influenced by orography (Siqueira et al., 2018). The second one is represented by rivers influenced by the presence of dams, which affect the sediment transport, such as the São Francisco, Jequitinhonha, Tocantins, Paraná, Salado, Madeira, Parnaíba and Doce rivers (See Figure 1 and Figure 4). The third one is for the stations having small drainage areas. For the latter situation, Figure 5 presents a detailed description of the modeling results that relate the drainage area of each station to the NSE and $BIAS$ values. It is noted that for areas larger than 100,000km², the $BIAS$ range is reduced (values between -67% and 200%), remaining mostly between -50 and 50% (Figure 5-b). For the NSE, most values are over -0.5 (Figure 5-a). Basins draining small Andean areas are very susceptible to landslides, delivering a large amount of sediments to the rivers (Restrepo et al., 2006; Martín-Vide et al., 2014). As mentioned before, MGB-SED AS does not explicitly represent landslide processes, showing low performance in these areas (e.g. headwaters of Magdalena, Bermejo and Pilcomayo rivers).

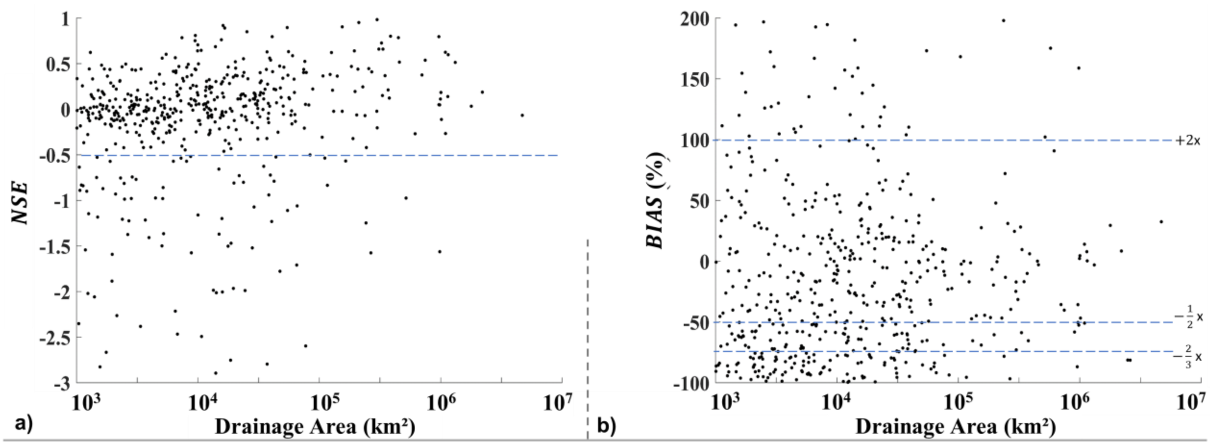

Figure 5: NSE and $BIAS$ (%) between observed and simulated QSS compared against the drainage area. Dashed blue lines in b) represent how much MGB-SED AS model over or underestimate QSS values.

Many stations that have small drainage areas are found in Colombia, for example. The results of Figure 4 in this region do not show a specific pattern, and the NSE and $BIAS$ values are sometimes negative, sometimes positive (see Figures S5, S6 and S7, Supporting Information). These basins also have high slope values and are characterized by the occurrence of strong storms (Restrepo et al., 2006). Also, sediment data from IDEAM are estimated by using a relationship between surface measurements and cross section measurements. This can be a source of uncertainties that must be taken into account when interpreting the results. The resolution of the models input data and the computational resources generally available make it difficult to represent these features in continental-scale models.

In Table S5 of the Supporting Information, we present an analysis of the model performance for several stations and the period when the model was calibrated (2002-2009) and the non-calibrated (1992-2001). The analysis shows that temporal extrapolation performed better than spatial extrapolation. The temporal extrapolation refers to the model evaluation for calibrated stations in another period. Spatial extrapolation refers to the model evaluation in the same period as the calibration, but for stations not used in that process.

4.1.2 Simulated data vs. other studies

The comparison between simulated annual QSS and estimated annual QSS by regional studies showed an R^2=0.87 (Figure 6-a). 61% of comparisons revealed that the MGB-SED AS estimates range between half and twice the values found in regional studies.

Figure 6-a also shows a trend for MGB-SED AS QSS to be lower than the regional studies QSS. Figure 6-b presents a comparison of $BIAS$ (MGB-SED SA and in-situ measured data) versus $Diff$ (MGB-SED SA and regional studies). The results indicate that the $BIAS$ and $Diff$ median were, respectively, -3% and -23%.

To understand the differences presented in the previous paragraph, we highlight that: i) the medians of $BIAS$ and NSE were, respectively, -3% and 0.11 for the 49 analyzed stations; ii) in the Altamira station, for example, the daily $BIAS$ and NSE were, respectively, 0% and 0.78, but in comparison with Filizola and Guyot (2009)study, the MGB-SED AS has estimated for this station QSS values 55% lower; iii) the regional studies (Table S1, Supporting Information) provided estimates using regression methods between QSS and water discharges. From the three points presented, we realize that MGB-SED AS had better agreement with in-situ data (for the most comparisons) than with estimated data from regional studies. Besides, the regression methods used in the aforementioned studies are simplified, and they consider some assumptions that may increase their estimates, such as: the use of few in-situ measured data, in which the majority belonging to the low-concentration period, to represent the temporal dynamics of sediments; Q enough to explain QSS; the increase of QSS is always increasing with Q. However, because of hysteresis effects, it is known that these premises often do not occur in nature, especially for large rivers, which is clearly demonstrated for the Amazon in studies performed by Bourgoin et al. (2007), Filizola et al. (2011) e Fassoni-Andrade and Paiva (2019). A broader discussion on this topic is presented in the next section.

The worst performance of MGB-SED AS was at Javari station (ID=45, Figure S2 and Table S1 - Supporting Information), where $BIAS$ and $Diff$ were, respectively, -95% and 92%. Javari station has a drainage area closer to 1×10^4 km² and the model calibration in the same sub-basin was performed by having focus on Solimões station (ID=47, Figure S2 - Supporting Information), which has a drainage area closer to 1×10^6 km². Situations like this show the difficulty to achieve a model with high performance to estimate daily QSS for all the continental domain and why the model has a better performance for stations with larger drainage areas (Figure 5).

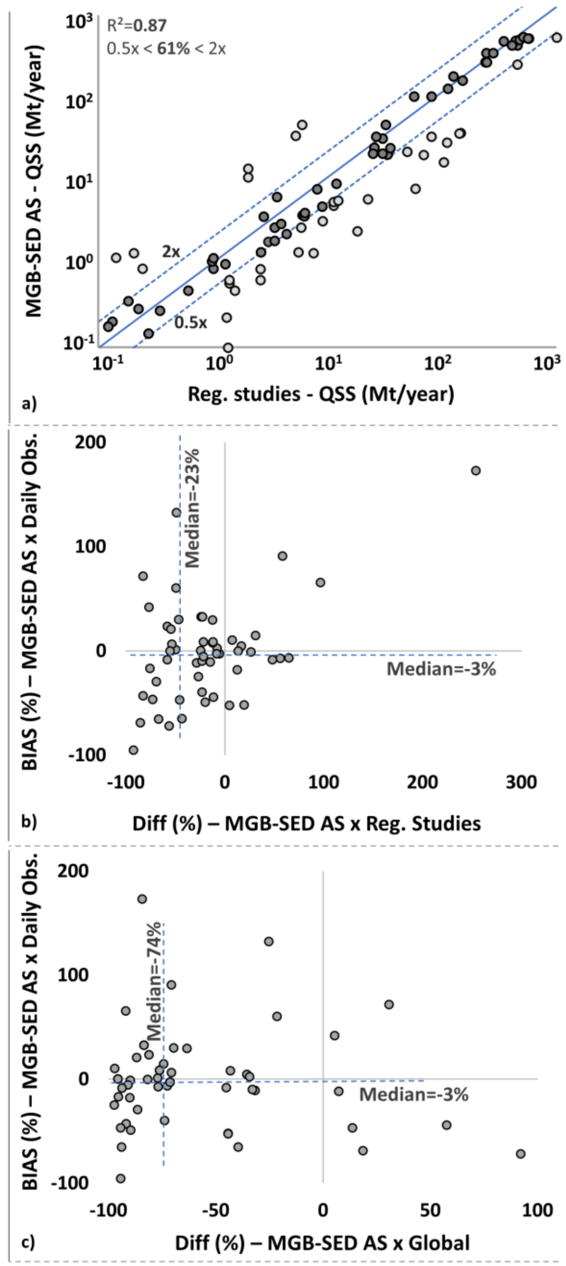

Figure 6: Performance of the MGB-SED AS model against in-situ observations, the results of regional and global studies. a) comparison between MGB-SED AS annual suspended sediment discharge (QSS) and QSS from regional studies; light gray dots refer to when the MGB-SED AS estimated more than double or less than half the regional studies values. b) comparison between daily simulated (MGB-SED AS) and observed (in-situ) QSS ($BIAS$) against annual simulated QSS (MGB-SED AS), and estimated from regional studies ($Diff$). c) comparison between daily simulated (MGB-SED AS) and observed (in-situ) QSS against annual simulated QSS from MGB-SED AS, and from the WBMsed global model (Cohen et al., 2014), using $BIAS$ and $Diff$, respectively. In figure b (c): a point exactly at the origin (x,y)=(0,0) means that both the results simulated by MGB-SED AS and those from regional studies (global model) have strong agreement with the in-situ observations; the point (x,y)=(-100,-100) means that the MGB-SED AS model had a poor performance compared to the observed data and a worse performance than the results of the regional studies (global model); the point (x,y)=(-100,0) means that the MGB-SED AS model performed better, if compared to the observed data, than the values estimated by regional studies (global model).

Figure 6-c presents a comparison between the results of MGB-SED AS and those of the WBMsed global model (Cohen et al., 2014). The median $Diff$ between the MGB-SED AS and the WBMsed model was -74%. It shows that the estimated values by MGB-SED SA are considerably lower than those predicted by WBMsed. In this case, although the WBMsed model does not consider only Q to estimate QSS, it is based on a global empirical equation, which may have limitations given the different variables around the globe.

After an analysis of Figure S2 and Table S2 (Supporting Information), no spatial pattern of the $Diff$ metric was found. WBMsed showed a tendency to overestimate both MGB-SED AS and in-situ measurements. This can be related to several aspects, like: i) differences in precipitation grids used by the models and their associated resolution; ii) differences in computing slopes, which can greatly affect the erosion rates (Garcia-Ruíz et al. 2015); iii) Muskingum-Cunge method to route the flow, which is not suitable to represent backwater and floodplain effects for several South America regions (e.g. Angarita et al., 2018; Bravo et al., 2012; Paiva et al., 2013, 2011; Pontes et al., 2017; Siqueira et al., 2018; Zhao et al., 2017) ; and iv) the QSS estimated by the WBMsed model was neither calibrated nor validated by Cohen et al. (2014) in SA. However, it is worth mentioning that the complexity of the WBMsed makes it difficult to accurately compare the factors that impact sediment estimates.

The tables used to generate Figure 6 graphics can be found on the Supporting Information (Table S1 and Table S2).

4.2 Analysis of Sediment Flows in South America

4.2.1 Time Series

Figure 7 presents the comparison between daily simulated and in-situ QSS data for several large South American rivers. The presented statistics were calculated considering only the values of observation dates. Apavi station, on the Magdalena river (Figure 7-1), offers a lot of observed data, and, in general, there was an agreement between the simulated and observed data ($BIAS$=-6% and NSE=0.29). In the Amazon basin, suspended sediments were well represented for several stations, which can be seen in the Fazenda Vista Alegre (Figure 7-3) and Altamira (Figure 7-3) stations. The latter had $BIAS$=0% and NSE=0.78. Óbidos station (Figure 7-2) show a $BIAS$ of 30%, while upstream station showed values closer to 0% (Figure 4-b). According to Filizola and Guyot, (2009), Óbidos station has a particular protocol, where sampling is taken only in the surface zone, underestimating the real concentration (Bouchez et al.,2011). This explain why Óbidos station has a $BIAS$ value in disagreement with their upstream stations. It is pointed out that the variability of the QSS estimated by the sediment model is strongly influenced by the variability of hydrological variables calculated by MGB AS (see Equation 1).

The impact of fluvial hydrodynamics on sediment transport can be observed at Fazenda Vista Alegre, Óbidos, Puerto Pilcomayo (Figure 7-8) and Brazo Largo (Figure 7-10) stations, where backwater effects and floodplain storage reduce the sediment transport by 16%, 13%, 55%, and 30%, respectively. In other places like Altamira (Figure 7-4) and Paraná (Figure 7-9) stations, sediment transport was reduced by 6%. These are regions where rivers generally have higher slopes and the effect of floodplains is less expressive. 36% of simulated river reaches showed sediment storage in floodplains greater than 1 t/year. More information about the importance of floodplains are presented in the next sections.

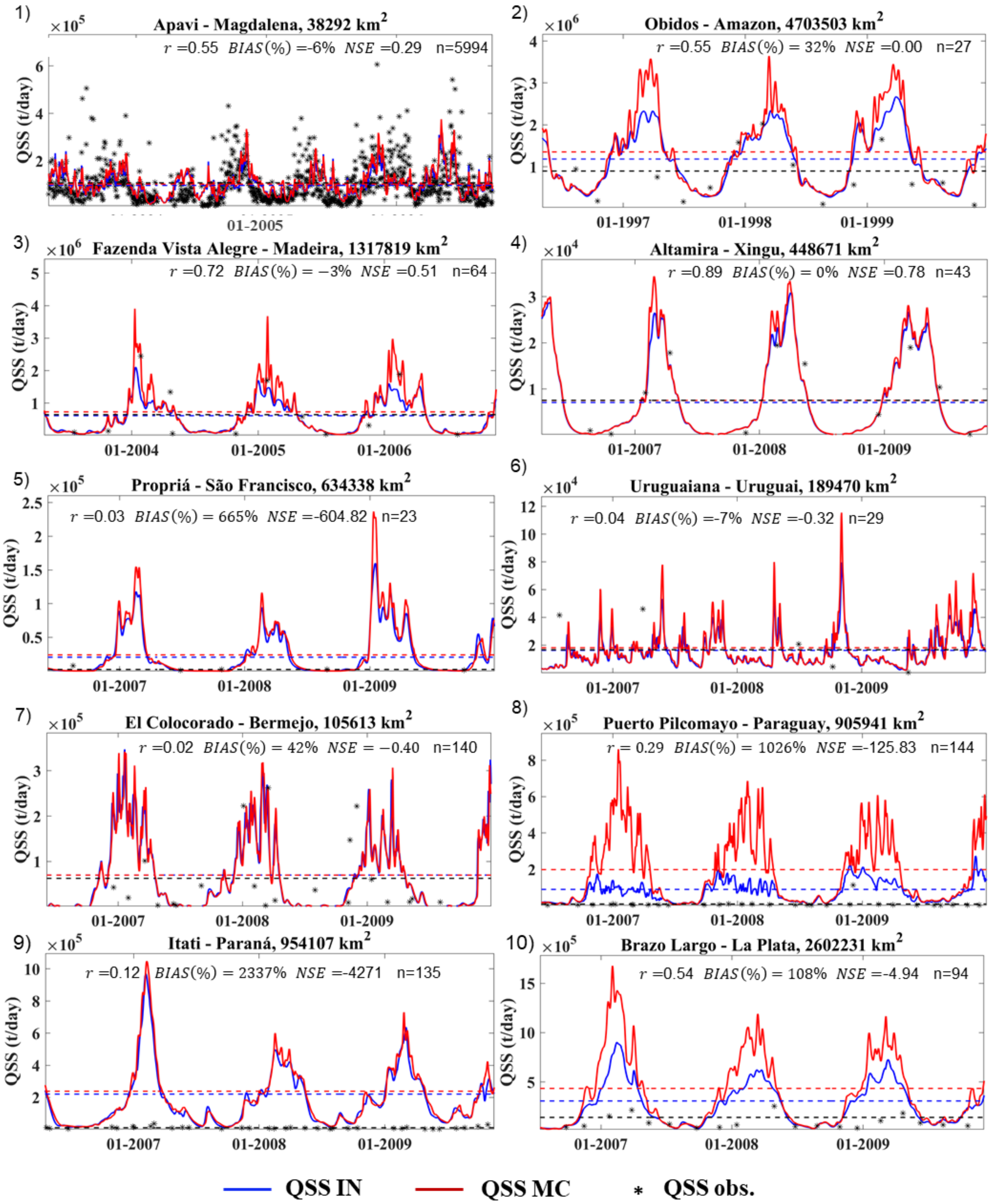

Figure 7: Comparison between observed (QSSobs - black asterisks) and simulated suspended sediment discharge (QSS) for some large rivers of South America. Model performance is presented in terms of correlation (r),

$BIAS$ (%) and Nash-Sutcliffe efficiency (NSE) for hydrodynamic modeling (QSS IN). Daily QSS simulated time series are presented for both inertial (QSS IN - blue lines) and Muskingum-Cunge (QSS MC – red lines) routing methods. Dashed lines show the respective long term averages. n is the number of observed QSS. The sediment stations locations are presented in Figure 8-a.

In the Propriá station, the $BIAS$ was 665%, and in-situ QSS values were always very low (Figure 7-5). In this case, as for other stations like Paraná ($BIAS$ 2337%, Figure 7-9), these low observed values are associated with sediment trap in large dams located upstream. Highlighting this phenomenon is important because, in these cases, the observed temporal dynamics are inconsistent with the simulated natural sediment discharge in the rivers.

The Puerto Pilcomayo station (Figure 7-8), in the Paraguay River, also showed low performance, which can be related to the difficulty of the MGB AS model to represent the strong deposition that occur in the Pilcomayo River (upstream the Pilcomayo, $BIAS$ has negative value). Due it and large impoundments in the Paraná River, MGB-SED AS overestimate the observed values of QSS in the outlet of the La Plata River (Figure 7-10)

In many places, the model estimates and in-situ observations did not match, which may have been caused by the non-representation of reservoirs in the modeling process. In the São Francisco River, sediment trapped by reservoirs may approach 70% (Creech et al., 2015). Syvitski et al. (2005), considering impoundments, estimated that sediment flows to the oceans in SA were reduced by about 13%/ year. The expectation of the construction of new dams in the SA and their impacts on water and sediment flows, mainly in the Amazon Basin (Latrubesse et al., 2017), have grown. Besides, studies like Dunn et al.(2018) and Dunn et al. (2019) have shown the importance of quantifying sediment flows in the present and future scenarios because large and important rivers around the world have stopped supplying their deltas.

Figures S8, S9 and S10 show the number of QSS observed data for each sediment station.

4.2.2 Spatial Analysis

Figure 8-a presents the long-term average annual QSS (t/year). From the simulated results, the Amazon River is the one with the highest QSS (4.36×10^8 t/year), followed by the Orinoco (1.37×10^8 t/year),La Plata (1.11×10^8 t/year) and Magdalena (3.26×10^7 t/year) rivers. The Magdalena carries a load for times greater than those carried by the São Francisco (7.46×10^6 t/year) and Tocantins (7.44×10^6 t/year) rivers, which have twice their drainage area. The average flows of the São Francisco and Tocantins rivers are 56% lower and 88% higher, respectively, than the Magdalena river. The Doce River transports a suspended load of 5.04×10^6 t/year, which is equivalent to 70% of the load carried by the Tocantins River, although the Doce River has a drainage area (flow) ten (fourteen) times smaller.

Andean rivers flowing to Pacific Ocean also exhibit high rates of sediment transport (QSS~10^7 t/year), except for dry regions like in the northern Chile. These Andean rivers show QSS values in the same order of São Francisco and Tocantins rivers (Figure 8-a), which places them among the main sediment transporters of the SA, although they drain a considerably smaller area.

The simulated QSS for the most downstream stations of each basin agreed with the observed values ($BIAS$ values, Figure 4). Figure 8-a represents a natural potential transport situation in the rivers, since a sediment trapping in dams was not considered in the sediment modeling. Rivers such as the São Francisco and Paraná, for example, currently have field clearer waters downstream from the dams in comparison to what is suggested by the sediment simulation.

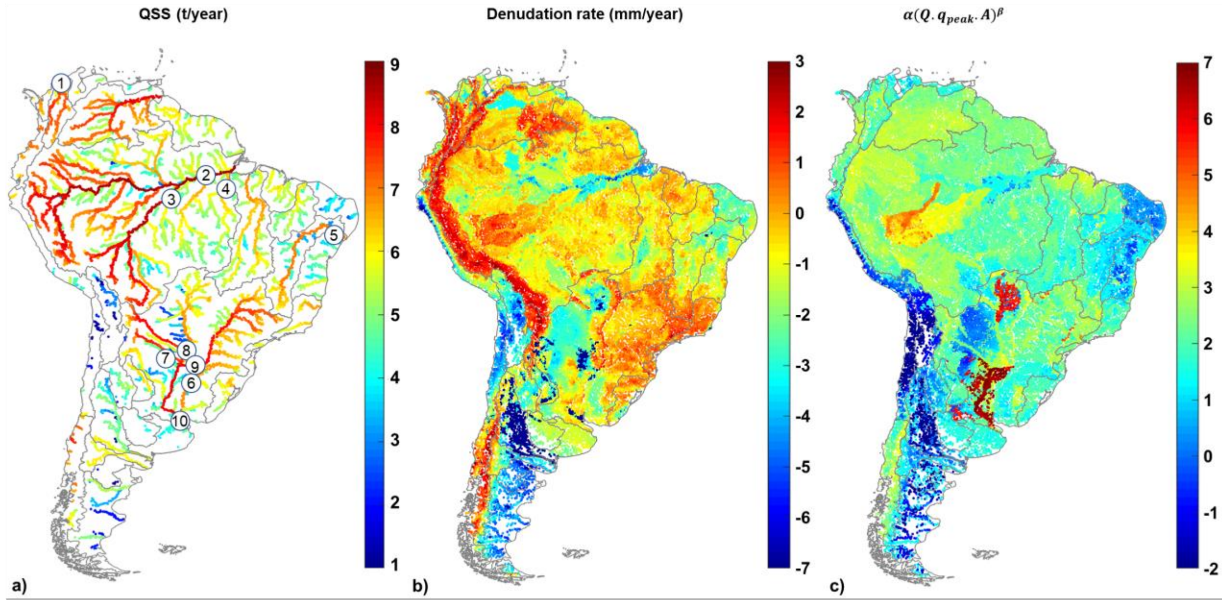

Figure 8: Average Annual a) suspended sediment discharge (QSS) over South America; b) denudation rate (silt+clay+sand); and c) $\alpha(Q.q_{peak}.A)\beta$. Colorbar values are in the logarithmic scale. Numbers in c) refer to stations showed in Figure 7.

Figure 8-b shows spatial patterns of denudation rates (soil loss in mm/year; sediment density equal to 2.65 t/m³ was used for the unit conversion, see Morris and Fan, 1998). The SA average value is 4.6 mm/year. With 16.62 mm/year, the Magdalena basin presented the highest mean denudation rate. The Amazon basin had the second-highest denudation rate of 6.8 mm/year. In the Solimões, Madeira and Juruá river basins, denudation rate was 16.15, 9.89 and 5.03 mm/year, respectively. For the Negro, Tapajós and Xingu watersheds, these values were 0.41, 0.40 and 0.28, respectively.

The high denudation rates calculated for the Magdalena and Amazon river basins are mainly associated with the high slopes and strong storm events in the Andean region (see Guyot et al., 1996; Restrepo et al., 2006). The Restrepo et al. (2006) analysis, between 1986 and 1996 using more than 30 stations, indicated an increasing trend of erosion in the Magdalena basin. Among the causes for this increase are catchments with small drainage areas having high relief and narrow alluvial plains, heavy precipitations, and changes in land use and land cover. Furthermore, compared to the Amazon, the Magdalena basin is more influenced by the Andes and has fewer flat regions (Figure 1). Paraguay (7.48 mm/year) and Orinoco (5.71 mm/year) also have high denudation rate values.

The Paraíba do Sul, Doce and the Paraná river basins also stand out with high denudation rates: 5.34 mm/year, 2.12 mm/year and 3.52 mm/year, respectively. These basins have a strongly undulating and hilly relief, soils covered mainly by agriculture and degraded pastures, and a very seasonal rainfall pattern, with heavy rainfall for the November-January period. Despite the Parnaíba and São Francisco river basins having a hilly relief, they are in a semi-arid region, for which lower denudation rates are estimated (0.28 mm/year and 0.85 mm/year, respectively).

The relations between denudation rate, slope (represented by the LS factor), and precipitation (represented by the Aridity index) are presented in Figure 9. Red dots in Figure 9-a and Figure 9-b, correspond to rivers for which the LS factor and Aridity Index are above the percentile 95%, respectively, which indicate steeper (Figure 9-a), and extremely dry (Figure 9-b) areas. This figure shows, in agreement with Figure 3 and Figure 8, that high denudation rates can occur for high and low slopes, and are found mainly in humid areas (Aridity Index <100, Figure 9-a), while arid regions always have very low denudation rates (Figure 9-b). Figure 9 shows that a pattern between the denudation rate, LS factor and aridity index does not exist. We expected this, since the model considers several processes based on what occurs in nature, and not only the water discharge, to estimate erosion and sediment transport. García-Ruiz et al. (2015) identified, from several studies around the world, that almost all erosion rates can occur for any climate condition. The authors also pointed out that a significant effect of the increase in erosion rates occurs as precipitation and slope rise. This increase tends to reach, on average, a limit when the slope and precipitation reach ±0.2m/m and ±1,400mm/year, respectively.

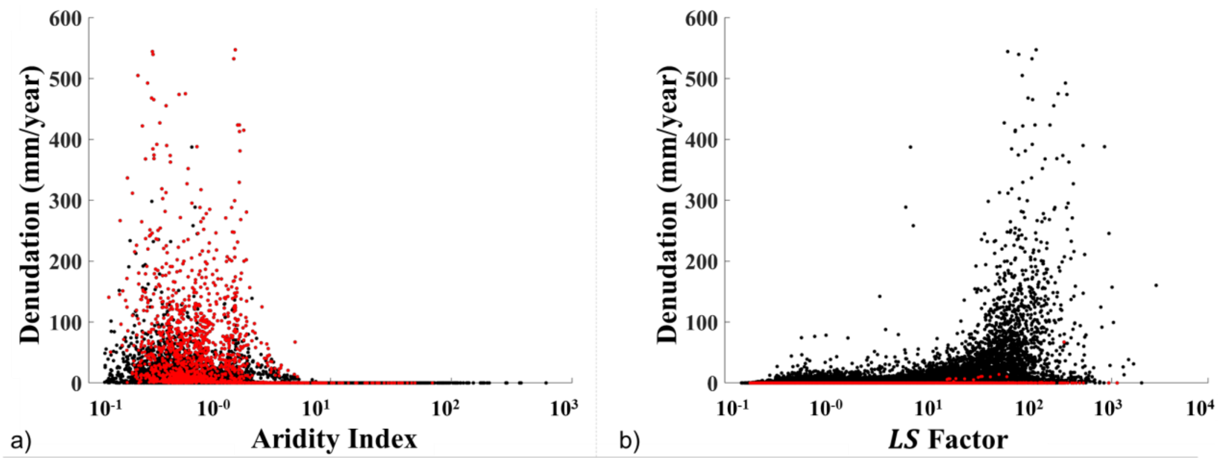

Figure 9: Denudation rate versus: a) Aridity Index (red dots represent LS values above the percentile 95%); b) LS factor (red dots represent Aridity Index values above the percentile 95%).

The MUSLE factor related to the ability to remove soil particles is the $\alpha(Q.q_{peak}.A)\beta$. In regions such as Brazilian northeast, Chaco, Atacama Desert, and others in the south of the continent (Desaguadero, Colorado and Negro river basins), the values of this factor are comparatively low concerning the rest of the SA. High values are found in the Pantanal, Purus River basin, part of the Juruá River basin, and in the lower La Plata river basin (Figure 8-c). It is noticeable that some spatial patterns presented in Figure 8-b are directly related to the standards presented in Figure 8-c, showing the influence of the $\alpha(Q.q_{peak}.A)\beta$ factor in the denudation rate.

In the Pantanal, Juruá River and Purus River, even the $\alpha(Q.q_{peak}.A)\beta$ factor values being higher, the simulated QSS tended to underestimate the observed values (Figure 4). Thus, we believe that these highlighted values may be related to the calibration parameters of the hydrological model and the spatial discretization performed by Siqueira et al. (2018), which was more focused on hydrological processes than sediment processes. Also, no pattern was observed in the maps of the input parameters (Figure 3) that could explain the observed pattern for the Purus and Juruá river basins in Figure 8-b. The high values in the La Plata river basin may be associated with large wetlands, which produces high runoff but low sediment yield.

4.2.3 Multiple relationships: water discharge, sediment concentration and deposition

4.2.3.1 Overview

Figure 10 shows SA rivers with the highest Q and SSC values according to the modeling results. The figure illustrates that largest SSC values in the Amazon basin are located in the upper Madeira River and other rivers having the headwaters in Andean regions, as already known by previous studies (Amsler and Drago, 2009; Cohen et al., 2014; Latrubesse et al., 2005). The pattern found in the river reaches with higher and lower concentrations in the central Amazon matches well with the results found by Fassoni-Andrade and Paiva (2019) using remote sensing. The greatest differences are found downstream of the confluence between the Amazon and Tapajós rivers, where the SSC (Figure 10) keeps decreasing, while Fassoni-Andrade and Paiva (2019) observed an increase downstream of the confluence with the Xingú River. The authors concluded that this difference could be associated with sediment resuspension caused by variations at the Amazon estuary, which are not represented in the MGB-SED AS model.

The Magdalena, Bermejo, Pilcomayo, and some rivers in the south of SA showed high concentrations. The Amazonian rivers without headwaters in the Andes have low SSC, such as the Negro, Tapajós and Xingu rivers (Figure 10), having high water discharge values (>9,700 m^3/s in average, see Filizola and Guyot, 2009).

According to MGB-SED AS simulations, 2×10^9 t/year of silt and clay leave the hillsides and reach the SA rivers. Of these, about 12% are trapped in the floodplains before reaching the Oceans under natural conditions (i.e., without impoundments). This value can be substantially higher for some regions. As related by Bourgoin et al. (2007) and most recently by Rudorff et al. (2018), the mean trap efficiency for the floodbasin encompassing the Lago Grande de Curuai (lower Amazon River) is 45%-48%. For this region, strong winds can induce waves resuspending fine sediment in dry seasons, when the floodplains and lakes are shallow (Bourgoin et al., 2007; Fassoni-Andrade and Paiva, 2019a; Schmidt, 1972), which means that less sediment is trapped. Despite the importance of the wind effect for this region, it was not considered in the current study. Meanwhile, for the central Amazon floodplains, the trapped value found is one order ($\sim10^7$ t/year) bigger than that estimated by Rudorff et al. (2018) only for one reach. It is not possible to make a direct comparison due to the different approaches used in the aforementioned studies.

The effect of SS deposition on the floodplains is quite evident in the highlands of Madeira river basin (Figure 10), causing a sharp reduction in SSC values from upstream to downstream. For example, Guyot et al. (1996), using regressions between observed Q and QSS data, estimated a reduction for QSS and SSC of 54% and 95%, respectively in the Mamoré basin. In comparison, we estimated a 35% (75%) increase (decrease) in QSS (SSC). As discussed in section 4.1.2, the main differences can be associated to the methods used to estimate QSS values (regression analysis × sediment modeling), which may be enough to find such different results and patterns.

The region assessed on the Mamoré River drains a large amount of sediment originating in the Andes. The same happens with the Pilcomayo River. The Mamoré River flows through regions with dynamic and complex fluvial geomorphology, with avulsion and silting mechanisms of the bed in the Llanos de Moxos floodplain. According to MGB-SED AS simulations, $\sim2\times10^7$ t/year of SS are deposited in this floodplain (Figure 10). The Pilcomayo

River flows through and floods the flat regions of the Chaco, losing water to the atmosphere through evapotranspiration (Martín-Vide et al., 2014). The Pilcomayo River basin also presents great complexities, similar to those described for the Mamoré River (see Martín-Vide et al., 2014). In the upper Pilcomayo, near the Andes, Martín-Vide et al. (2014) estimated a mean SSC of 15×10³mg/L, while SCC simulated was 28×10³mg/L. For Pilcomayo station, Martín-Vide et al. (2014) estimate a QSS of 140 Mt/year, while for the same station ($BIAS$=-20% and NSE=0.23), MGB-SED AS estimate was 96 Mt/year. Guyot et al. (1996) estimated a mean SSC of 13×10³mg/L in Abapo (Figure 10), about two times higher than estimated by MGB-SED AS (6×10³ mg/L) and by Buarque (2015), in which it was found 5×10³ mg/L (personal communication) using a regional model.

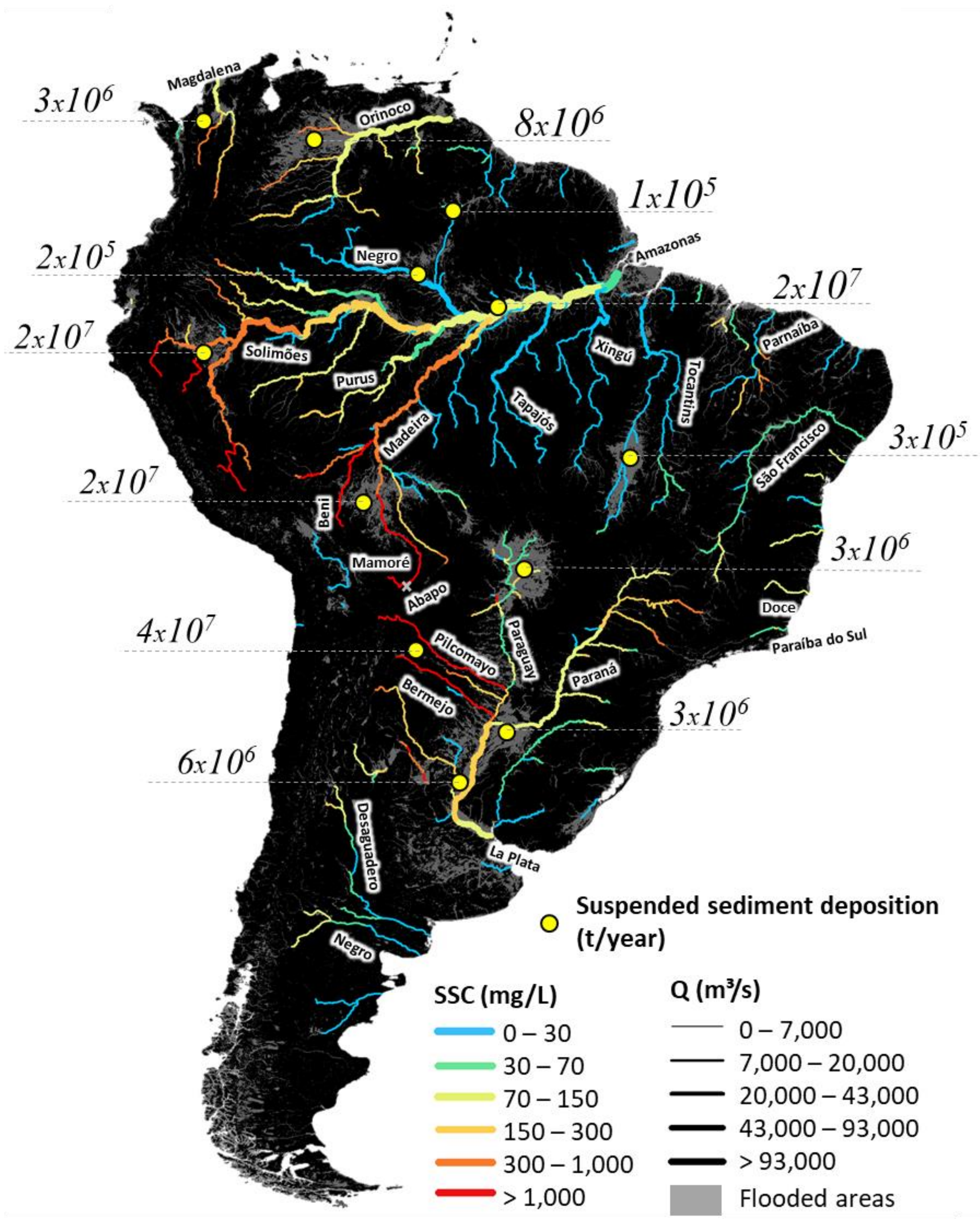

Figure 10: Annual average of suspended sediment load deposited in the main floodplains of South America; long-term daily average of suspended sediment concentration (SSC) and water discharge (Q) for main large rivers. Flooded areas were acquired from Fluet-Chouinard et al. (2015).

MGB-SED SA has estimated lower SSC values in the Mamoré River when compared to Guyot et al. (1996) estimates. The main differences found could be related to the following aspects: i) there was difficulty in calibrating the continental-scale model in the regions of upper Madeira, with the available data; ii) the processes observed in the Andean region, such as landslide-driven sediment flux, are not well represented in the proposed modeling as discussed by Buarque (2015), which shows that significant uncertainties for these regions may exist. The same can occur for other Andes regions, like the headwater of the Pilcomayo, Bermejo and Magdalena rivers.

The Pilcomayo River was the only river that showed an increase in concentrations from upstream to downstream (Figure 10). It happens because simulated Q values increase from the upstream to the middle Pilcomayo and decrease again next to the outlet. Martín-Vide et al. (2014) noted that the increase in Q is not proportional to the SSC for the Pilcomayo River. This behavior was identified using MGB-SED AS for the Mamoré River, which differs from the approach used by Guyot et al. (1996). Using the MGB-SED model, which considers several processes and variables and not only Q to estimate the QSS, Buarque (2015) found a NSE=0.7 in the Fazenda Vista Alegre station (Madeira River). This indicates that the connection suggested in some studies (e.g. Filizola and Guyot, 2009; Guyot et al., 1996; Lima et al., 2005; Meade et al., 1990; Restrepo et al., 2006), that QSS always increases with Q, cannot always be applied.

The assessment in large flooded areas (Figure 10) indicated that 57% of the total SS trapped in the floodplains is deposited in these places. The plains having the highest amounts of deposited SS are the Banãdo La Estrella (4 $\times 10^7$ t/year), Llanos de Moxos (2×10^7 t/year), central Amazon floodplains (2×10^7 t/year) and the interfluvial floodplains of Peru (2×10^7 t/year). In the whole Amazon basin, about 1×10^8 t/year of SS are deposited in floodplains, which corresponds to ~50% of total SS trapped in the floodplains in the whole South America.

4.2.3.2 Annual Sediment Balance

The impact of model calibration and hydrodynamic routing in South America was also assessed by the suspended loads leaving the continent. When using the hydrodynamic model without calibration, the QSS reaching the oceans was 2.86×10^9 t/year. After calibration, this value was 1.00×10^9 t/year, which means that the calibration of MGB-SED AS provided estimates 65% lower. When the calibration and Muskingum-Cunge routing method were considered, the value increased by 18% (1.18×10^9 t/year). Syvitski et al. (2005) estimated for "prehuman" period that QSS delivered from SA was, on average 2.68×10^9 t/year, a value 268% (6%) higher (lower) than estimated with calibrated (non-calibrated) MGB-SED AS. In their global study on tropical rivers, Syvitski et al. (2014) highlighted that most modeling projects use boundary conditions without considering sediment depositions in the deltas, which could reduce the value of the SS that effectively leaves the continent. In this paper, we partially represent this effect, since the model does not consider coastal basins and islands with A<1,000km² or submerged coastal regions.

Naturally (without considering impoundments), the daily water (SS) transport of 3.10×10^{10} m³ (2.76×10^6 t) by the SA rivers to the oceans was estimated using MGB-SED AS. Of this total, 57% (43%) of the water (SS) volume comes from the Amazon basin.

Figure 11 presents a monthly balance of SS and Q for South America and several of its major rivers. In addition, to expand the understanding of the different relations between Q and SSC, a map with the Delay Index (DI) calculated between these two variables is also presented in this figure. Values in red (blue) shades show how many days the SSC peak is ahead (behind) in relation to the Q peak.

The *DI* map (Figure 11) shows that the occurrence of the SSC peak earlier than the Q peak is mainly in some Amazon tributaries, Brazilian northeast and areas closer to Atacama Desert. In the Paraná, São Francisco (Figure 11-f), Bermejo, Magdalena (Figure 11-b), Doce (Figure 11-g), and Paraíba do Sul river basins, *DI* values are closer to zero. A common feature of these basins is that they have hilly relief regions and relatively few flat areas, which facilitates the transport of water and sediments to (and along) river channels.

Throughout the year, the simulated QSS in SA ranged 3-7×10^7 t/day, in which higher values were occurring between February and June (Figure 11-d). The SS deposition on the floodplains has higher values between November and April.

In the Amazon River, the sediment supply (MUSLE) peak was in January, together with the floodplains deposition (Dep) peak, and the QSS peak only occurs in February (Figure 11-a). The Amazon River dynamics is mainly influenced by lateral contributions, which is related to the variation of the rainy periods in the south and north of the basin (Villar et al., 2008). In the south, there is the Madeira River basin with high sediment yield (44% of all Amazonas) and the occurrence of QSS and Q peaks, respectively, in February and April. In the north, there is the Negro River with low sediment yield (1.5% of all Amazonas) and the occurrence of QSS and Q peaks, respectively, in June and July. The Solimões and Madeira rivers is those one that, in fact, control the temporal dynamics of the Amazon River in the outlet. In the Solimões river, the discharge, sediment supply and deposition of SS occur concomitantly in March. Both SSC (Figure 10) and QSS decrease from upstream to downstream in Amazon basin (Solimões-Amazon rivers). The QSS and SSC back to increase from the confluence with Madeira River.

The Magdalena River showed two Q peaks (Figure 11-b), where the first peaks are about two months apart (May-July) and the last in about one month (November-December). SS (discharge, sediment supply and deposition on floodplains) also have two peaks, occurring in May and in November, concomitantly with Q peaks. In the La Plata River, the Q and QSS peaks were observed in March and February, respectively. The SS supply peak was observed in February, and about 10% of these sediments are then deposited on floodplains, in which the deposition peak occurs in January (Figure 11-c).

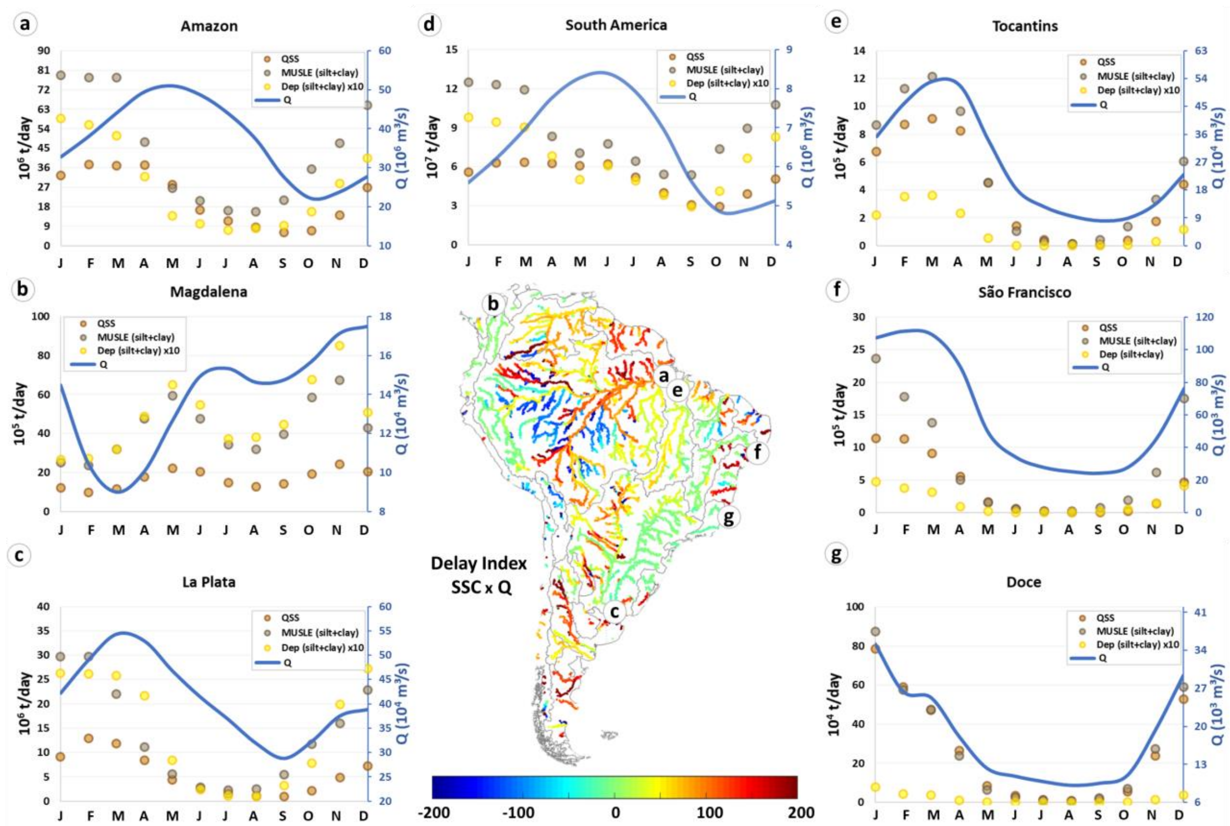

Figure 11: Annual sediment balance for South America and some large rivers. Figures a-g show water discharge (Q) in blue lines, suspended sediment load estimated with MUSLE equation in gray circles, suspended sediment discharge (QSS) in brownish circles, and suspended sediment deposited in floodplains (Dep) in yellow circles. Dep values are one order bellow other sediment values, so in the figure, we raised the values tenfold. The central map shows de Delay Index, calculated between de suspended sediment concentration (SSC) and Q. Reddish (blue) values show how many days the SSC peak is ahead (delayed) in relation to the Q peak.

The Tocantins (Figure 11-e) and São Francisco (Figure 11-f) river basins have a similar area, are geographic close to each other but have very different sediment flows. The Tocantins River (Figure 11-e) has a large floodplain on the Araguaia River, while the São Francisco River has almost no floodplains (Figure 1). Despite this, the São Francisco river basin has a more deposited SS load than that of Tocantins. This occurs because the São Francisco transports a larger load with lower flows, which facilitates deposition and because the Araguaia River has a lower sediment yield in its headwaters (Figure 8-a). The SS supply, floodplains deposition and transport occur in January to the São Francisco and in March to the Tocantins.

The Doce River presents a straightforward relationship between water discharge and sediments, and similar monthly variations (Figure 11-g). The Q and QSS peaks occur in January, and only about 0.6% of the sediments reaching the drainage network (this value can be zero for dry season) are deposited in floodplains.

Figure 11 shows that in basins with larger flat areas (e.g., Magdalena, Amazonas and La Plata), the SS supply peak occurs concomitantly with the deposition peak. In the Doce and São Francisco river basins, the SS supply peak occurs together with the deposition and also Q peaks. It means that only for the highest flows the SS reach the floodplains of these basins. In the

Tocantins river basin, this fact may be related to the low sediment transport in the Araguaia River, which is the main tributary and has the largest flat regions.

5 Conclusions

In this research, we performed the coupling of the MGB-SED sediment model with the hydrologic-hydrodynamic model of South America (MGB AS). From this coupling, the MGB-SED AS was developed and assessed. Using the model results was possible to investigate and understand temporal and spatial patterns of suspended sediment (SS) flows on a continental scale.

The main conclusions related to the process of development, performance evaluation, and application of the model for the comprehension of continental standards are:

- The MGB-SED AS model was able to perform accurate estimates at several sites, which was evaluated against in-situ measurements. The calibration of the model parameters improved the estimates of the SS flows, obtaining an export value from SA, under natural conditions (without impoundments), equivalent to 65% of the values estimated without calibration.
- The use of the hydrodynamic routing method enabled better SS estimates, especially the simulated QSS peaks in places having floodplains. By using the simplified routing method and without floodplains, estimates of annual loads have increased by 18%.
- We observed that the MGB-SED AS results agreed with in-situ observed QSS. The model tends to estimate QSS values smaller than with the estimates from regional studies and the global model used as comparison. The use of the continental model does not exclude the use of models at regional and local scales for smaller-scale studies.
- The Amazon (4.36×10^8 t/year), Orinoco (1.37×10^8 t/year), La Plata (1.11×10^8 t/year) and Magdalena (3.26×10^7) rivers presented the highest suspended sediment yield, meaning 44%, 14%, 11% and 3% of total South America discharges values to the ocean. Floodplains play an important role by retaining about 12% (2.40×10^8 t/year) of SS carried by the rivers. About 57% of the total deposition occurs in large flooded areas, for which the Banãdo La Estrella (4×10^7 t/year), Llanos de Moxos (2×10^7 t/year), central Amazon floodplains (2×10^7 t/year) and the interfluvial floodplains of Peru (2×10^7 t/year) representing the four regions with the highest deposition rates.
- The increase in Q does not always result in an increase in SSC/QSS. Especially in rivers with large floodplains, Q and SSC/QSS peaks can occur up to months apart.
- Catchments with higher slopes and higher rainfall have higher SSC, while QSS tends to be higher where flows are higher.

Results presented in this work enabled the comprehension of the spatiotemporal dynamics of SS flows in South America. Generated maps present the annual rates of denudation, transport (discharge and concentration), and deposition (in the plains) of SS throughout the continent. Charts of the annual sediment balance were also generated for some rivers chosen as having high sediment transport. These information may be useful for other studies on a continental scale, for example, related to reservoirs, fish productivity, nutrient transport, carbon balance, and other studies related to ecosystem maintenance and soil conservation. Besides, this information can support decision making, planning, and management of continental land use. Studies such as that of Latrubesse et al. (2017) have shown a possible increase of dams in South America in the future. Thus, to have a better knowledge of sediment fluxes in the present, it is necessary to consider these structures in sediment modeling, which is part of the continuation of this research.

Acknowledgments

The first and second authors thanks the Brazilian CNPq (*Conselho Nacional de Desenvolvimento Científico e Tecnológico*) for supporting this research under the Grants Number 167867/2018-0 and 305636/2019-7.

Some datasets for this research are included in this paper: Siqueira et al. (2018).

In-situ data supporting this research are available in http://www.snirh.gov.br/hidroweb/ (ANA), http://bdhi.hidricosargentina.gob.ar/ (BDHI) and http://www.ideam.gov.co/ (IDEAM).

Data information

Simulated Suspended Sediment Discharge for South America Rivers (MGB-SED AS) - V1.0 are available in: doi:10.17632/k7c5482fsm.1

References

Aguiar, A.P.D., Vieira, I.C.G., Assis, T.O., Dalla-Nora, E.L., Toledo, P.M., Oliveira Santos-Junior, R.A., Batistella, M., Coelho, A.S., Savaget, E.K., Aragão, L.E.O.C., Nobre, C.A., Ometto, J.P.H., 2016. Land use change emission scenarios: Anticipating a forest transition process in the Brazilian Amazon. Glob. Chang. Biol. 22, 1821–1840. https://doi.org/10.1111/gcb.13134

Alewell, C., Borrelli, P., Meusburger, K., Panagos, P., 2019. Using the USLE: Chances, challenges and limitations of soil erosion modelling. Int. Soil Water Conserv. Res. 7, 203–225. https://doi.org/10.1016/j.iswcr.2019.05.004

Almagro, A., Oliveira, P.T.S., Nearing, M.A., Hagemann, S., 2017. Projected climate change impacts in rainfall erosivity over Brazil. Sci. Rep. 7, 1–12. https://doi.org/10.1038/s41598-017-08298-y

Almeida, R.M., Tranvik, L., Huszar, V.L.M., Sobek, S., Mendonça, R., Barros, N., Boemer, G., Arantes, J.D., J., Roland, F., 2015. Phosphorus transport by the largest Amazon tributary (Madeira River, Brazil) and its sensitivity to precipitation and damming. Inl. Waters 5, 275–282.

Amsler, M., Prendes, H., 2000. El Río Paraná en su Tramo Medio, in: Transporte de Sedimentos y Processos Fluviales Asociados. pp. 233–306.

Amsler, M.L., Drago, E.C., 2009. A review of the suspended sediment budget at the confluence of the Paran´a and Paraguay Rivers. Hydrol. Process. An Int. J. 23, 3230–3235. https://doi.org/10.1002/hyp

Andreadis, K.M., Schumann, G.J.P., Pavelsky, T., 2013. A simple global river bankfull width and depth database. Water Resouces Res.

Angarita, H., Wickel, A.J., Sieber, J., Chavarro, J., Maldonado-Ocampo, J.A., Herrera-R, G.A., Delgado, J., Purkey, D., 2018. Basin-scale impacts of hydropower development on the Mompós Depression wetlands, Colombia. Hydrol. Earth Syst. Sci. 22, 2839–2865. https://doi.org/10.5194/hess-22-2839-2018

Aragão, L.E.O.C., 2012. The rainforest ' s water pump. Nature 489, 217–218.

Arnold, J.G., Srinivasan, R., Muttiah, R.S., Williams, J.R., 1998. Large area hydrologic modeling and assessment part I: model development. J. Am. Water Resour. Assoc. https://doi.org/10.1111/j.1752-1688.1998.tb05961.x

Bates, P.D., Horritt, M.S., Fewtrell, T.J., 2010. A simple inertial formulation of the shallow water equations for efficient two-dimensional flood inundation modelling. J. Hydrol. 387, 33–45. https://doi.org/10.1016/j.jhydrol.2010.03.027

Bates, P.D., Neal, J., Sampson, C., Smith, A., Trigg, M., 2018. Progress Toward Hyperresolution Models of Global Flood Hazard. Risk Model. Hazards Disasters 211–232. https://doi.org/doi.org/10.1016/B978-0-12-804071-3.00009-4

Beck, H.E., van Dijk, A.I.J.M., de Roo, A., Dutra, E., Fink, G., Orth, R., Schellekens, J., 2017. Global evaluation of runoff from 10 state-of-the-art hydrological models. Hydrol. Earth Syst. Sci. 21, 2881–2903.

Beighley, R.E., Gummadi, V., 2011. Developing channel and floodplain dimensions with limited data: A case study in the Amazon Basin. Earth Surf. Process. Landforms 36, 1059–1071.

Benavidez, R., Jackson, B., Maxwell, D., Norton, K., 2018. A review of the (Revised) Universal Soil Loss Equation ((R)USLE): With a view to increasing its global applicability and improving soil loss estimates. Hydrol. Earth Syst. Sci. 22, 6059–6086. https://doi.org/10.5194/hess-22-6059-2018

Best, J., 2019. Anthropogenic stresses on the world's big rivers. Nat. Geosci. 12, 7–21. https://doi.org/10.1038/s41561-018-0262-x

Beusen, A.H.W., Dekkers, A.L.M., Bouwman, A.F., Ludwig, W., Harrison, J., 2005. Estimation of global river transport of sediments and associated particulate C, N, and P. Global Biogeochem. Cycles 19. https://doi.org/10.1029/2005GB002453

Bierkens, M.F.P., 2015. Global hydrology 2015: State, trends, and directions. Water Resouces Res. 51, 4923–4947. https://doi.org/10.1002/2015WR017173.Received

Borrelli, P., Robinson, D.A., Fleischer, L.R., Lugato, E., Ballabio, C., Alewell, C., Meusburger, K., Modugno, S., Schütt, B., Ferro, V., Bagarello, V., Oost, K. Van, Montanarella, L., Panagos, P., 2017. An assessment of the global impact of 21st century land use change on soil erosion. Nat. Commun. 8, 1–13. https://doi.org/10.1038/s41467-017-02142-7

Bourgoin, L.M., Bonnet, M.P., Martinez, J.M., Kosuth, P., Cochonneau, G., Moreira-Turcq, P., Guyot, J.L., Vauchel, P., Filizola, N., Seyler, P., 2007. Temporal dynamics of water and sediment exchanges between the Curuaí floodplain and the Amazon River, Brazil. J. Hydrol. 335, 140–156. https://doi.org/10.1016/j.jhydrol.2006.11.023

Bravo, J.M., Allasia, D., Paz, a. R., Collischonn, W., Tucci, C.E.M., 2012. Coupled Hydrologic-Hydraulic Modeling of the Upper Paraguay River Basin. J. Hydrol. Eng. 17, 635–646. https://doi.org/10.1061/(ASCE)HE.1943-5584.0000494

Brêda, J.P.L.F., Paiva, R.C.D., Collischon, W., Bravo, J.M., Siqueira, V.A., Steinke, E.B., 2020. Climate change impacts on South American water balance from a continental-scale hydrological model driven by CMIP5 projections. Clim. Change. https://doi.org/10.1007/s10584-020-02667-9

Buarque, D.C., 2015. Simulação da geração e do transporte de sedimetnos em grandes bacias: estudo de caso do rio Madeira. Universidade Federal do Rio Grande do Sul, Porto Alegre, Tese (Doutorado em Recursos Hídricos e Saneamento Ambiental).

Campagnoli, F., 2006. The production of the sediment of the South America continent: propose of mapping of the erosion rates based on geological and geomorphological aspects. Rev. Bras. Geomorfol.

Cohen, S., Kettner, A.J., Syvitski, J.P.M., 2014. Global suspended sediment and water discharge dynamics between 1960 and 2010: Continental trends and intra-basin sensitivity. Glob. Planet. Change 115, 44–58. https://doi.org/10.1016/j.gloplacha.2014.01.011

Cohen, S., Kettner, A.J., Syvitski, J.P.M., Fekete, B.M., 2013. WBMsed, a distributed global-scale riverine sediment flux model: Model description and validation. Comput. Geosci. 53, 80–93. https://doi.org/10.1016/j.cageo.2011.08.011

Collischonn, W., Allasia, D., Da Silva, B.C., Tucci, C.E.M., 2007. The MGB-IPH model for large-scale rainfall—runoff modelling. Hydrol. Sci. J. 52, 878–895. https://doi.org/10.1623/hysj.52.5.878

Creech, C.T., Siqueira, R.B., Selegean, J.P., Miller, C., 2015. Anthropogenic impacts to the sediment budget of São Francisco River navigation channel using SWAT. Int. J. Agric. Biol. Eng. 8, 1–20. https://doi.org/10.3965/j.ijabe.20150803.1372

Dearing, J.A., Jones, R.T., 2003. Coupling temporal and spatial dimensions of global sediment flux through lake and marine sediment records. Glob. Planet. Change 39, 147–168. https://doi.org/10.1016/S0921-8181(03)00022-5

Doetterl, S., Van Oost, K., Six, J., 2012. Towards constraining the magnitude of global agricultural sediment and soil organic carbon fluxes. Earth Surf. Process. Landforms 37, 642–655. https://doi.org/10.1002/esp.3198

Dunn, F.E., Darby, S.E., Nicholls, R.J., Cohen, S., Zarfl, C., Fekete, B.M., 2019. Projections of declining fluvial sediment delivery to major deltas worldwide in response to climate change and anthropogenic stress. Environ. Res. Lett. 14, 084034. https://doi.org/10.1088/1748-9326/ab304e

Dunn, F.E., Nicholls, R.J., Darby, S.E., Cohen, S., Zarfl, C., Fekete, B.M., 2018. Projections of historical and 21st century fluvial sediment delivery to the Ganges-Brahmaputra-Meghna, Mahanadi, and Volta deltas. Sci. Total Environ. 642, 105–116. https://doi.org/10.1016/j.scitotenv.2018.06.006

Fagundes, H. de O., Fan, F.M., Paiva, R.C.D., 2019. Automatic calibration of a large-scale sediment model using suspended sediment concentration, water quality, and remote sensing data. Brazilian J. Water Resour. 24, 1–18. https://doi.org/10.1590/2318-0331.241920180127

Fagundes, H.O., Paiva, R.C.D., Fan, F.M., Buarque, D.C., Fassoni-Andrade, A.C., 2020. Sediment modeling of a large-scale basin supported by remote sensing and in-situ observations. Catena 190, 104535. https://doi.org/10.1016/j.catena.2020.104535

Fan, F.M., Buarque, D.C., Pontes, P.R.M., Collischonn, W., 2015. Um Mapa de Unidades de Resposta Hidrológica para a América do Sul. XXI Simpósio Bras. e Recur. Hídricos 1–8.

FAO/UNESCO, 1974. FAO/UNESCO Soil Map of the World | Food and Agriculture Organization of the United Nations [WWW Document]. FAO/UNESCO Soil Map World.

Fassoni-Andrade, A.C., Paiva, R.C.D. de, 2019a. Mapping spatial-temporal sediment dynamics of river-floodplains in the Amazon. Remote Sens. Environ. 221, 94–107. https://doi.org/10.1016/j.rse.2018.10.038

Fassoni-Andrade, A.C., Paiva, R.C.D. de, 2019b. Mapping spatial-temporal sediment dynamics of river-floodplains in the Amazon. Remote Sens. Environ. 221, 94–107.

https://doi.org/10.1016/j.rse.2018.10.038

Filizola, N., Guyot, J.-L., Wittmann, H., Martinez, J.-M., de, E., 2011. The Significance of Suspended Sediment Transport Determination on the Amazonian Hydrological Scenario. Sediment Transp. Aquat. Environ. https://doi.org/10.5772/19948

Filizola, N., Guyot, J.L., 2011. Fluxo de sedimentos em suspensão nos rios da Amazônia. Rev. Bras. Geociências 41, 566–576.

Filizola, N., Guyot, J.L., 2009. Suspended sediment yields in the Amazon basin: an assessment using the Brazilian national data set. Hydrol. Process. 23, 3207–3215. https://doi.org/10.1002/hyp.7394 Suspended

Fleischmann, A., Collischonn, W., Paiva, R., Tucci, C.E., 2019a. Modeling the role of reservoirs versus floodplains on large-scale river hydrodynamics. Nat. Hazards 99, 1075–1104. https://doi.org/10.1007/s11069-019-03797-9

Fleischmann, A., Paiva, R., Collischonn, W., 2019b. Can regional to continental river hydrodynamic models be locally relevant? A cross-scale comparison. J. Hydrol. X 3, 100027. https://doi.org/10.1016/j.hydroa.2019.100027

Fleischmann, A., Siqueira, V., Paris, A., Collischonn, W., Paiva, R., Pontes, P., Crétaux, J.F., Bergé-Nguyen, M., Biancamaria, S., Gosset, M., Calmant, S., Tanimoun, B., 2018. Modelling hydrologic and hydrodynamic processes in basins with large semi-arid wetlands. J. Hydrol. 561, 943–959. https://doi.org/10.1016/j.jhydrol.2018.04.041

Fluet-Chouinard, E., Lehner, B., Rebelo, L.M., Papa, F., Hamilton, S.K., 2015. Development of a global inundation map at high spatial resolution from topographic downscaling of coarse-scale remote sensing data. Remote Sens. Environ. 158, 348–361. https://doi.org/dx.doi.org/10.1016/j.rse.2014.10.015

Föeger, L.B., 2019. Modelagem Hidrossedimentológica de Grandes Bacias com Propagação Inercial de Vazão: estudo de caso da baica do rio Madeira. Federal University of Espirito Santo.

Forsberg, B.R., Melack, J.M., Dunne, T., Barthem, R.B., Goulding, M., Paiva, R.C.D., Sorribas, M. V., Silva, U.L., Weisser, S., 2017. The potential impact of new Andean dams on Amazon fluvial ecosystems, PLoS ONE. https://doi.org/10.1371/journal.pone.0182254

Galy, V., Peucker-Ehrenbrink, B., Eglinton, T., 2015. Global carbon export from the terrestrial biosphere controlled by erosion. Nature 521, 204–207. https://doi.org/10.1038/nature14400

García-Ruiz, J.M., Beguería, S., Nadal-Romero, E., González-Hidalgo, J.C., Lana-Renault, N., Sanjuán, Y., 2015. A meta-analysis of soil erosion rates across the world. Geomorphology 239, 160–173. https://doi.org/10.1016/j.geomorph.2015.03.008

Getirana, A.C. V, Paiva, R.C.D., 2013. Mapping large-scale river flow hydraulics in the Amazon Basin. Water Resour. Res. 49, 2437–2445. https://doi.org/10.1002/wrcr.20212

Grill, G., Lehner, B., Thieme, M., Geenen, B., Tickner, D., Antonelli, F., Babu, S., Borrelli, P., Cheng, L., Crochetiere, H., Ehalt Macedo, H., Filgueiras, R., Goichot, M., Higgins, J., Hogan, Z., Lip, B., McClain, M.E., Meng, J., Mulligan, M., Nilsson, C., Olden, J.D., Opperman, J.J., Petry, P., Reidy Liermann, C., Sáenz, L., Salinas-Rodríguez, S., Schelle, P., Schmitt, R.J.P., Snider, J., Tan, F., Tockner, K., Valdujo, P.H., van Soesbergen, A., Zarfl, C., 2019. Mapping the world's free-flowing rivers. Nature 569, 215–221. https://doi.org/10.1038/s41586-019-1111-9

Guyot, J., Bourges, J., Calle, H., Cortes, J., Hoorelbecke, R., Roche, M., 1989. Transport of suspended sediments to the Amazon by the Andean river: The River Mamore, Bolivia, in: Fourth International Symposium on River Sedimentation. ISRS, Beijing, China. pp. 106–

113.
Guyot, J.L., Filizola, N., Quintanilla, J., Cortez, J., 1996. Dissolved solids and suspended sediment yields in the Rio Madeira basin, from the Bolivian Andes to the Amazon. IAHS-AISH Publ. 236, 55–63.
Guyot, J.L., Jouanneau, J.M., Wasson, J.G., 1999. Characterisation of river bed and suspended sediments in the Rio Madeira drainage basin (Bolivian Amazonia). J. South Am. Earth Sci. 12, 401–410. https://doi.org/10.1016/S0895-9811(99)00030-9
Hanasaki, N., Kanae, S., Oki, T., 2006. A reservoir operation scheme for global river routing models. J. Hydrol. 327, 22–41.
Hanasaki, N, Kanae, S., Oki, T., Masuda, K., Motoya, K., Shirakawa, N., Shen, Y., Tanaka, K., 2008. An integrated model for the assessment of global water resources – Part 1: Model description and input meteorological forcing. Hydrol. Earth Syst. Sci. 12, 1007–1025.
Hanasaki, N., Kanae, S., Oki, T., Masuda, K., Motoya, K., Shirakawa, N., Shen, Y., Tanaka, K., 2008. An integrated model for the assessment of global water resources – Part 2: Applications and assessments. Hydrol. Earth Syst. Sci. 12, 1027–1037.
Hanasaki, N., Yoshikawa, S., Pokhrel, Y., Kanae, S., 2018. A global hydrological simulation to specify the sources of water used by humans. Hydrol. Earth Syst. Sci. 22, 789–817.
IDEAM, 2007. Protocolo para el monitoreo y seguimiento del agua.
International Standard - ISO, n.d. Measurement of liquid flow in open channels - Methods for measurement of characteristics of suspended sediment.
Ito, A., 2007. Simulated impacts of climate and land-cover change on soil erosion and implication for the carbon cycle, 1901 to 2100. Geophys. Res. Lett. https://doi.org/10.1029/2007GL029342
Kettner, A.J., Restrepo, J.D., Syvitski, J.P.M., 2010. A spatial simulation experiment to replicate fluvial sediment fluxes within the Magdalena River Basin, Colombia. J. Geol. 118, 363–379. https://doi.org/10.1086/652659
Knisel, W.G., 1980. CREAMS: A Field-Scale Model for Chemicals, Runoff and Erosion for Agricultural Management Systems.
Kollat, J.B., Reed, P.M., Wagener, T., 2012. When are multiobjective calibration trade-offs in hydrologic models meaningful? Water Resour. Res. 48, 1–19. https://doi.org/10.1029/2011WR011534
Kouwen, N., Soulis, E.D., Pietroniro, A., Donald, J., HARRINGTON; R. A, 1993. Grouped Response Units for Distributed Hydrologic Modeling. J. Water Resour. Plan. Manag. 119, 289–305.
Krysanova, V., Mu, D., Becker, A., 1998. Development and test of a spatially distributed hydrological/ water quality model for mesoscale watersheds. Ecol. Model 106, 261–289.
Kuhn, N.J., Hoffmann, T., Schwanghat, W., Dotterwiech, M., 2009. Agricultural soil erosion and global carbon cycle: controversy over? Earth Surf. Process. Landforms 34, 1033–1038. https://doi.org/10.1002/esp
Lal, R., 2003. Soil erosion and the global carbon budget. Environ. Int. 29, 437–450. https://doi.org/10.1016/S0160-4120(02)00192-7
Latrubesse, E.M., Arima, E.Y., Dunne, T., Park, E., Baker, V.R., D'Horta, F.M., Wight, C., Wittmann, F., Zuanon, J., Baker, P.A., Ribas, C.C., Norgaard, R.B., Filizola, N., Ansar, A., Flyvbjerg, B., Stevaux, J.C., 2017. Damming the rivers of the Amazon basin. Nature 546, 363–369. https://doi.org/10.1038/nature22333
Latrubesse, E.M., Stevaux, J.C., Sinha, R., 2005. Tropical rivers. Geomorphology 70, 187–206.

https://doi.org/10.1016/j.geomorph.2005.02.005

Lehner, B., Liermann, C.R., Revenga, C., Vörömsmarty, C., Fekete, B., Crouzet, P., Döll, P., Endejan, M., Frenken, K., Magome, J., Nilsson, C., Robertson, J.C., Rödel, R., Sindorf, N., Wisser, D., 2011. High-resolution mapping of the world's reservoirs and dams for sustainable river-flow management. Front. Ecol. Environ. 9, 494–502. https://doi.org/10.1890/100125

Lehner, B., Verdin, K., Jarvis, A., 2008. New global hydrography derived from spaceborne elevation data. Eos (Washington. DC). 89, 93–94. https://doi.org/https://doi.org/10.1029/2008EO100001

Lima, J.E.F.W., Lopes, W.T. a., De Oliveira Carvalho, N., Vieira, M.R., Da Silva, E.M., 2005. Suspended sediment fluxes in the large river basins of Brazil. IAHS ICCE Symp. Sediments Budgets 1 1, 355–364.

Littleboy, M., Silburn, M.D., Freebairn, D.M., Woodruff, D.R., Hammer, G.L., Leslie, J.K., 1992. Impact of soil erosion on production in cropping systems. I. Development and validation of a simulation model. Aust. J. Soil Res. 30, 757–774.

Martín-Vide, J.P., Amarilla, M., Zárate, F.J., 2014. Collapse of the Pilcomayo River. Geomorphology 205, 155–163. https://doi.org/10.1016/j.geomorph.2012.12.007

Meade, R.H., Weibezahn, F.H., Lewis Jr, W.M., Hernandez, D.P., 1990. Suspended-sediment budget for the Orinoco River., in: The Orinoco River as an Ecosystem. pp. 55–79.

Morehead, M.D., Syvitski, J.P., Hutton, E.W.H., Peckham, S.D., 2003. Modeling the temporal variability in the flux of sediment from ungauged river basins. Glob. Planet. Change 39, 95–110. https://doi.org/10.1016/S0921-8181(03)00019-5

Morris, G., Fan, J., 1998. Reservoir Sedimentation Handbook. McGraw-Hill Book Co., New York.

Mouyen, M., Longuevergne, L., Steer, P., Crave, A., Lemoine, J.M., Save, H., Robin, C., 2018. Assessing modern river sediment discharge to the ocean using satellite gravimetry. Nat. Commun. 9, 1–9. https://doi.org/10.1038/s41467-018-05921-y

Müller-Nedebock, D., Chaplot, V., 2015. Soil carbon losses by sheet erosion: A potentially critical contribution to the global carbon cycle. Earth Surf. Process. Landforms 40, 1803–1813. https://doi.org/10.1002/esp.3758

Murphy, J., 2019. Declining suspended sediment in United States rivers and streams: Linking sediment trends to changes in land use/cover, hydrology and climate. Hydrol. Earth Syst. Sci. Discuss. 1–37. https://doi.org/10.5194/hess-2019-435

Naipal, V., Ciais, P., Wang, Y., Lauerwald, R., Guenet, B., Van Oost, K., 2018. Global soil organic carbon removal by water erosion under climate change and land use change during AD-1850-2005. Biogeosciences 15, 4459–4480. https://doi.org/10.5194/bg-15-4459-2018

Naipal, V., Reick, C., Pongratz, J., Van Oost, K., 2015. Improving the global applicability of the RUSLE model - Adjustment of the topographical and rainfall erosivity factors. Geosci. Model Dev. 8, 2893–2913. https://doi.org/10.5194/gmd-8-2893-2015

Nash, J.E., Sutcliffe, J. V, 1970. River Flow Forecasting Through Conceptual Models Part I-a Discussion of Principles. J. Hydrol. 10, 282–290. https://doi.org/10.1016/0022-1694(70)90255-6

New, M., Lister, D., Hulme, M., Makin, I., 2002. A high-resolution data set of surface climate over global land areas. Clim. Res. 21, 1–25.

Niu, B., Hong, S., Yuan, J., Peng, S., Wang, Z., Zhang, X., 2014. Global trends in sediment-related research in earth science during 1992-2011: A bibliometric analysis. Scientometrics

98, 511–529. https://doi.org/10.1007/s11192-013-1065-x

O'Loughlin, F.E., Paiva, R.C.D., Durand, M., Alsdorf, D.E., Bates, P.D., 2016. A multi-sensor approach towards a global vegetation corrected SRTM DEM product. Remote Sens. Environ. 182, 49–59.

Oliveira, P.T.S., Nearing, M.A., Wendland, E., 2015. Orders of magnitude increase in soil erosion associated with land use change from native to cultivated vegetation in a Brazilian savannah environment. Earth Surf. Process. Landforms 40, 1524–1532. https://doi.org/10.1002/esp.3738

Paiva, R.C.D., Buarque, D.C., Collischonn, W., Bonnet, M.P., Frappart, F., Calmant, S., Bulh??es Mendes, C.A., 2013. Large-scale hydrologic and hydrodynamic modeling of the Amazon River basin. Water Resour. Res. 49, 1226–1243. https://doi.org/10.1002/wrcr.20067

Paiva, R.C.D., Collischonn, W., Tucci, C.E.M., 2011. Large scale hydrologic and hydrodynamic modeling using limited data and a GIS based approach. J. Hydrol. 406, 170–181. https://doi.org/10.1016/j.jhydrol.2011.06.007

Panagos, P., Borrelli, P., Meusburger, K., Yu, B., Klik, A., Lim, K.J., Yang, J.E., Ni, J., Miao, C., Chattopadhyay, N., Sadeghi, S.H., Hazbavi, Z., Zabihi, M., Larionov, G.A., Krasnov, S.F., Gorobets, A. V., Levi, Y., Erpul, G., Birkel, C., Hoyos, N., Naipal, V., Oliveira, P.T.S., Bonilla, C.A., Meddi, M., Nel, W., Al Dashti, H., Boni, M., Diodato, N., Van Oost, K., Nearing, M., Ballabio, C., 2017. Global rainfall erosivity assessment based on high-temporal resolution rainfall records. Sci. Rep. 7, 1–12. https://doi.org/10.1038/s41598-017-04282-8

Panagos, P., Borrelli, P., Poesen, J., Ballabio, C., Lugato, E., Meusburger, K., Montanarella, L., Alewell, C., 2015. The new assessment of soil loss by water erosion in Europe. Environ. Sci. Policy 54, 438–447. https://doi.org/10.1016/j.envsci.2015.08.012

Pelletier, J.D., 2012. A spatially distributed model for the long-term suspended sediment discharge and delivery ratio of drainage basins. J. Geophys. Res. Earth Surf. 117, 1–15. https://doi.org/10.1029/2011JF002129

Phinzi, K., Ngetar, N.S., 2019. The assessment of water-borne erosion at catchment level using GIS-based RUSLE and remote sensing: A review. Int. Soil Water Conserv. Res. https://doi.org/10.1016/j.iswcr.2018.12.002

Pontes, P.R.M., 2016. Modelagem hidrológica e hidrodinâmica integrada da bacia do Prata. Universidade Federal do Rio Grande do Sul.

Pontes, P.R.M., Fan, F.M., Fleischmann, A.S., Paiva, R.C.D., Buarque, D.C., Siqueira, V.A., Jardim, P.F., Sorribas, M.V., Collischonn, W., 2017. MGB-IPH model for hydrological and hydraulic simulation of large floodplain river systems coupled with open source GIS. Environ. Model. Softw. 94, 1–20.

Restrepo, J.D., Kjerfve, B., Hermelin, M., Restrepo, J.C., 2006. Factors controlling sediment yield in a major South American drainage basin: The Magdalena River, Colombia. J. Hydrol. 316, 213–232. https://doi.org/10.1016/j.jhydrol.2005.05.002

Rivera, I.A., Cardenas, E.A., Espinoza-Villar, R., Espinoza, J.C., Molina-Carpio, J., Ayala, J.M., Gutierrez-Cori, O., Martinez, J.M., Filizola, N., 2019. Decline of fine suspended sediments in the Madeira River basin (2003-2017). Water (Switzerland) 11. https://doi.org/10.3390/w11030514

Rudorff, C.M., Dunne, T., Melack, J.M., 2018. Recent increase of river–floodplain suspended sediment exchange in a reach of the lower Amazon River. Earth Surf. Process. Landforms

43, 322–332. https://doi.org/10.1002/esp.4247
Sadeghi, S.H.R., Gholami, L., Khaledi Darvishan, A., Saeidi, P., 2014. A review of the application of the MUSLE model worldwide. Hydrol. Sci. J. 59, 365–375. https://doi.org/10.1080/02626667.2013.866239
Santini, W., Camenen, B., Le Coz, J., Vauchel, P., Guyot, J.-L., Lavado, W., Carranza, J., Paredes, M.A., Pérez Arévalo, J.J., Arévalo, N., Espinoza Villar, R., Julien, F., Martinez, J.-M., 2019. An index concentration method for suspended load monitoring in large rivers of the Amazonian foreland. Earth Surf. Dyn. 7, 515–536. https://doi.org/10.5194/esurf-2018-93
Sartori, M., Philippidis, G., Ferrari, E., Borrelli, P., Lugato, E., Montanarella, L., Panagos, P., 2019. A linkage between the biophysical and the economic: Assessing the global market impacts of soil erosion. Land use policy 86, 299–312. https://doi.org/10.1016/j.landusepol.2019.05.014
Schmidt, G.W., 1972. Amounts of suspended solids and dissolved substances in the middle reaches of the Amazon over the course of one year. Amazoniana 3, 208–223.
Shen, Z.Y., Chen, L., Chen, T., 2012. Analysis of parameter uncertainty in hydrological modeling using GLUE method: a case study of SWAT model applied to Three Gorges Reservoir Region, China. Hydrol. Earth Syst. Sci. Discuss. 8, 8203–8229. https://doi.org/10.5194/hessd-8-8203-2011
Shin, S., Pokhrel, Y., Miguez-Macho, G., 2019. High-resolution modeling of reservoir release and storage dynamics at the continental scale. Water Resouces Res. 55, 787–810.
Siqueira, V.A., Paiva, R.C.D., Fleischmann, A.S., Fan, F.M., Anderson, L., Pontes, P.R.M., Paris, A., Calmant, S., Collischonn, W., 2018. Toward continental hydrologic – hydrodynamic modeling in South America. Hydrol. Earth Syst. Sci. 22, 4815–4842. https://doi.org/doi.org/10.5194/hess-22-4815-2018
Syvitski, J.P.M., Cohen, S., Kettner, A.J., Brakenridge, G.R., 2014. How important and different are tropical rivers? - An overview. Geomorphology 227, 5–17. https://doi.org/10.1016/j.geomorph.2014.02.029
Syvitski, J.P.M., Milliman, J.D., 2007. Geology, Geography, and Humans Battle for Dominance over the Delivery of Fluvial Sediment to the Coastal Ocean. J. Geol. 115, 1–19. https://doi.org/10.1086/509246
Syvitski, J.P.M., Vörösmarty, C.J., Kettner, A.J., Green, P., 2005. Impact of Humans on the Flux of Terrestrial Sediment to the Global Coastal Ocean. Science (80-.). 308, 376–380.
Tan, Z., Leung, L.R., Li, H., Tesfa, T., Vanmaercke, M., Poesen, J., Zhang, X., Lu, H., Hartmann, J., 2017. A Global Data Analysis for Representing Sediment and Particulate Organic Carbon Yield in Earth System Models. Water Resour. Res. 53, 10674–10700. https://doi.org/10.1002/2017WR020806
Tan, Z., Leung, L.R., Li, H.Y., Tesfa, T., 2018. Modeling Sediment Yield in Land Surface and Earth System Models: Model Comparison, Development, and Evaluation. J. Adv. Model. Earth Syst. 10, 2192–2213. https://doi.org/10.1029/2017MS001270
van Beek, L.P.H., Wada, Y., Bierkens, M.F.P., 2011. Global monthly water stress: 1. Water balance and water availability. Water Resouces Res. 47. https://doi.org/doi:10.1029/2010WR009791
Van Oost, K., Quine, T.A., Govers, G., De Gryze, S., Six, J., Harden, J.W., Ritchie, J.C., McCarty, G.W., Heckrath, G., Kosmas, C., Giraldez, J. V., Marques Da Silva, J.R., Merckx, R., 2007. The impact of agricultural soil erosion on the global carbon cycle. Science (80-.).

318, 626–629. https://doi.org/10.1126/science.1145724
Villar, J.C.E., Ronchail, J., Guyot, J.L., Cochonneau, G., Filizola, N., Lavado, W., de Oliveira, E., Pombosa, R., Vauchel, P., 2008. Spatio-temporal rainfall variability in the Amazon basin countries (Brazil, Peru, Bolivia, Colombia, and and Ecuador). Int. J. Climatol. 2009, 1574–1594. https://doi.org/10.1002/joc
Wada, Y., Wisser, D., Bierkens, M.F.P., 2014. Global modeling of withdrawal, allocation and consumptive use of surface water and groundwater resources. Earth Syst. Dyn. Discuss. 5, 15–40.
Wang, Z., Van Oost, K., 2019. Modeling global anthropogenic erosion in the Holocene. Holocene 29, 367–379. https://doi.org/10.1177/0959683618816499
Willenbring, J.K., Von Blanckenburg, F., 2010. Long-term stability of global erosion rates and weathering during late-Cenozoic cooling. Nature 465, 211–214. https://doi.org/10.1038/nature09044
Williams, J.R., 1995. The EPIC model, in: Computer Models of Watershed Hydrology. pp. 909–1000.
Williams, J.R., 1975. SEDIMENT ROUTING FOR AGRICULTURAL WATERSHEDS '. Water Resour. Bull. 11.
Wischmeier, W., Smith, D., 1978. Predicting rainfall erosion losses: a guide to conservation planning, U.S. Department of Agriculture Handbook No. 537. https://doi.org/10.1029/TR039i002p00285
Wisser, D., Fekete, B.M., Vörösmarty, C.J., Schumann, A.H., 2010. Reconstructing 20th century global hydrography: A contribution to the Global Terrestrial Network- Hydrology (GTN-H). Hydrol. Earth Syst. Sci. 14, 1–24. https://doi.org/10.5194/hess-14-1-2010
Wood, E.F., Roundy, J.K., Troy, T.J., van Beek, L.P.H., Bierkens, M.F.P., Blyth, E., et al, 2011. Hyperresolution global land surface modeling: meeting a grand challenge for monitoring Earth's terrestrial water. Water Resour. Res. 47, 1–10.
Wu, W., Wang, S.S.Y., 2006. Formulas for sediment porosity and settling velocity. J. Hydraul. Eng. 132, 858–862.
Wuepper, D., Borrelli, P., Finger, R., 2019. Countries and the global rate of soil erosion. Nat. Sustain. 1–5. https://doi.org/10.1038/s41893-019-0438-4
Xiong, M., Sun, R., Chen, L., 2019. A global comparison of soil erosion associated with land use and climate type. Geoderma 343, 31–39. https://doi.org/10.1016/j.geoderma.2019.02.013
Xiong, M., Sun, R., Chen, L., 2018. Effects of soil conservation techniques on water erosion control: A global analysis. Sci. Total Environ. 645, 753–760. https://doi.org/10.1016/j.scitotenv.2018.07.124
Yamazaki, D., de Almeida, G.A.M., Bates, P.D., 2013. Improving computational efficiency in global river models by implementing the local inertial flow equation and a vector-based river network map. Water Resouces Res. 49, 7221–7235.
Yamazaki, D., Kanae, S., Kim, H., Oki, T., 2011. A physically based description of floodplain inundation dynamics in a global river routing model. Water Resouces Res. 47.
Yang, C.T., 1973. Incipient motion and sediment transport. J. Hydraul. Eng 10, 1679–1704.
Yang, D., Kanae, S., Oki, T., Koike, T., Musiake, K., 2003. Global potential soil erosion with reference to land use and climate changes. Hydrol. Process. 17, 2913–2928. https://doi.org/10.1002/hyp.1441
Yapo, P.O., Gupta, H.V., Sorooshian, S., 1998. Multi-objective global optimization for hydrologic models. J. Hydrol. 204, 83–97. https://doi.org/10.1016/S0022-1694(97)00107-8

Zhang, K., Douglas, B.C., Leatherman, S.P., 2004. Global warming and coastal erosion. Clim. Change 64, 41–58. https://doi.org/10.1023/B:CLIM.0000024690.32682.48

Zhao, F., Veldkamp, T.I.E., Frieler, K., Schewe, J., Ostberg, S., Willner, S., Schauberger, B., Gosling, S.N., Schmied, H.M., Portmann, F.T., Leng, G., Huang, M., Liu, X., Tang, Q., Hanasaki, N., Biemans, H., Gerten, D., Satoh, Y., Pokhrel, Y., Stacke, T., Ciais, P., Chang, J., Ducharne, A., Guimberteau, M., Wada, Y., Kim, H., Yamazaki, D., 2017. The critical role of the routing scheme in simulating peak river discharge in global hydrological models. Environ. Res. Lett. 12. https://doi.org/10.1088/1748-9326/aa7250

Water Resources Research

Supporting Information for

Sediment flows in South America supported by daily hydrologic-hydrodynamic modeling

H. O. Fagundes[1], F. M. Fan1, R. C. D. Paiva[1], V. A. Siqueira[1], D. C. Buarque[2], L. W. Kornowski[1], L. Laipelt[1], W. Collischonn[1]

[1]Institute of Hydraulic Research, Federal University of Rio Grande do Sul, Porto Alegre, Rio Grande do Sul, Brazil

[2]Department of Environmental Engineering, Federal University of Espírito Santo, Vitória, Espírito Santo, Brazil

Contents of this file

Introduction

This supporting information presents a detailed description of the MGB-SED model (Text S1), developed by Buarque (2015) and complementary results to those presented in the main text: the value of C-factor used in the sediment modeling (Figure S1); the sites used in the comparisons between MGB-SED AS model and other studies (Figure S2); model performance using KGE, $DCPerm$ and $RMSErel$ metrics (Figure S3); Detailed view of the MGB-SED AS performance in terms of r, $BIAS$ and NSE (Figures S4-S6); Scatter plot using all observed values against simulated values in the same days (Figure S7); number of samples for each in-situ sediment station (Figures S8-S9); values of suspended sediment discharge from MGB-SED AS and other studies for specific sites (Table S1 and S2); errors of model sediment balance (Table S3); Ranking of of South American rivers with highest annual QSS (Table S4); and performance analysis considering temporal and spatial extrapolations (Table S5).

Text S1. MGB-SED Equations

Basin Module

The Modified Universal Soil Loss Equation (MUSLE, Williams, 1975) is given by:

$$Sed = \alpha.(Q_{sur} * q_{peak} * A)^{\beta}.K.C.P.LS_{2D} \tag{1}$$

where Sed[t/day] is the sediment yield, Q_{sur}[mm/day] is the specific runoff volume, q_{peak}[m^3/s] is the peak runoff rate, A[ha] is the unit catchment area, K[0.013.t.m^2.h./m^3.t.cm] is the soil erodibility factor, C[-] is the cover and management practices factor, P[-] is the conservation practices factor, LS_{2D}[-] is a bidimensional topographic factor; and α and β are the fit coefficients of the equation (which are calibrated afterward), whose values originally estimated by Williams (1975) were 11.8 and 0.56, respectively.

The q_{peak} is estimated as a function of the area A and of the daily runoff volume Q_{sur}:

$$q_{peak} = \frac{Q_{sur}.A}{86400} \tag{2}$$

The K factor is estimated from equation proposed by Williams (1995) (Equation 3), which is detailed in Buarque (2015):

$$K = Fag.Fcs.Forg.Fa \tag{3}$$

, where Fag is a factor that gives low soil erodibility factors for soils with high coarse-sand contents and high values for soils with little sand, Fcs is a factor that gives low soil erodibility factors for soils with high clay to silt ratios, $Forg$ is a factor that reduces soil erodibility for soils with high organic carbon content, and Fa is a factor that reduces soil erodibility for soils with extremely high sand contents. These factors are calculated by Williams (1995):

$$Fag = 0.2 + 0.3 \cdot exp\left[-0.0256 \cdot SAN \cdot \left(1 - \frac{SIL}{100}\right)\right] \tag{4}$$

$$Fcs = \left(\frac{SIL}{ARG + SIL}\right)^{0.3} \tag{5}$$

$$Forg = 1 - \frac{0.25 \cdot orgC}{orgC + exp(3.72 - 2.95 \cdot orgC)} \tag{6}$$

$$Fa = 1 - \frac{0.7 \cdot \left(1 - \frac{SAN}{100}\right)}{\left(1 - \frac{SAN}{100}\right) + exp\left[-5.51 + 22.9 \cdot \left(1 - \frac{SAN}{100}\right)\right]} \quad (7)$$

, where SAN, SIL, ARG and $orgC$ are the percentages of sand, silt, clay and organic carbon, respectively.

To compute LS_{2D} factor, a routine was created by Buarque (2015). For each pixel $k\langle l, c\rangle$ of Digital Elevation Model (DEM), LS is computed automatically. The L factor is obtained based on Desmet & Govers (1996), using the unit contributing area concept (Kirkby & Chorley, 1967). This two-dimensional approach explicitly considers the convergence of the flow and, based on field observations, and it was able to consider not only the processes of erosion in the rill and interrill, but also the erosion in ephemeral ravines (Desmet & Govers, 1997). The L factor equation applied for each DEM pixel $k\langle l, c\rangle$ is:

$$L_k = \frac{\left(Am_k + Lp_k^2\right)^{m+1} - Am_k^{m+1}}{Lp^{m+2} \cdot Xdir_k^m \cdot (22{,}13)^m} \quad (7)$$

, where L [-] is the length factor of pixel k; Am [m^2] the accumulated drainage area in the pixel entrance; Lp [m] the pixel width; $Xdir$ [-] is an aspect direction factor for the pixel; m [-] is the exponent of the slope length. The direction factor $Xdir$ correspond to the distance between two neighboring pixels, defined as 1 when the direction between them is orthogonal or $\sqrt{2}$ when the direction is diagonal. The m index is acquired by expressions bellow:

$$m = \begin{vmatrix} 0{,}2 & se & Sf < 1 \\ 0{,}3 & se & 1 \le Sf < 3 \\ 0{,}4 & se & 3 \le Sf < 5 \\ 0{,}5 & se & Sf \ge 5 \end{vmatrix} \quad (8)$$

,where Sf [%] is the pixel slope. The Sf measure the rate of change of the elevation in the direction of the highest slope and is computed in the model for each pixel using the z [m] elevations of the four neighbors in the orthogonal directions, following the equation 9 (Wilson & Gallant, 2000):

$$Sf = \sqrt{\left(\frac{\partial z}{\partial x}\right)^2 + \left(\frac{\partial z}{\partial y}\right)^2} \quad (9)$$

,where $\partial z/\partial x$ e $\partial z/\partial y$ are the first-order partial differential that describes the rate of local variation of elevation z [m] against the orthogonal distances x and y. These differentials are calculated using finite centered difference:

$$\frac{\partial z}{\partial x} \approx \frac{z_l^{c+1} - z_l^{c-1}}{2 \cdot Lp}, \frac{\partial z}{\partial y} \approx \frac{z_{l+1}^{c} - z_{l-1}^{c}}{2 \cdot Lp} \quad (10)$$

$$\frac{\partial z}{\partial y} \approx \frac{z_{l+1}^{c} - z_{l-1}^{c}}{2 \cdot Lp} \quad (11)$$

,where l and c are the row and column that determine the pixel position in the matrix $k\langle l, c\rangle$. Pixel slope also can be estimated using the modified method proposed by Pradhan et al. (2006), based on the scaling of the slope, estimated from fractal theory, proposed by Zhang et al. (1999). More details see Naipal et al. (2015).

The slope factor S is computed using the equation proposed by Wischmeier & Smith (1978):

$$S_k = 65{,}41 \cdot \sin^2(\theta_k) + 4{,}56 \cdot \sin(\theta_k) + 0{,}065 \quad (12)$$

, where θ is the value of Sf in degrees.

The total volume of sediment generated in each Hydrological Response Unit (HRU) and stored in the linear reservoir is computed as follows:

$$SED_{i,j}^{t} = VSED_{i,j}^{t-1} + \sum_{k=1}^{NP_j} SED_{i,j}^{k} \quad (13)$$

,where $VSED$[t] is the volume in sediment reservoir of j HRU of i unit catchment, NP is the number of pixels of HRU, the indexes t and $t-1$ designate the current and previous time steps.

The total load discharge QS [t/s] of linear reservoir output is computed as a linear function of the respective stored load and delay time ŧ [s] of the surface reservoir. QS is computed by equation 14:

$$QS_{i,j}^{t} = \frac{1}{ŧ} VSED_{i,j}^{t} \quad (14)$$

The total sediment delivered in each unit catchment is divided into three fractions: silt, clay and sand. Each one is defined according to its percentage in the upper layer of each HRU soil type. The delivery of the three classes of particles each unit catchment to the stream network is calculated by:

$$SEDsil_i^t = \sum_{j=1}^{N_{URH}} \left(QS_{i,j}^t \cdot FRAC_{i,j}^t \cdot SIL_j\right) \cdot \Delta t \tag{15}$$

$$SEDarg_i^t = \sum_{j=1}^{N_{URH}} \left(QS_{i,j}^t \cdot FRAC_{i,j}^t \cdot ARG_j\right) \cdot \Delta t \tag{16}$$

$$SEDsan_i^t = \sum_{j=1}^{N_{URH}} \left(QS_{i,j}^t \cdot FRAC_{i,j}^t \cdot SAN_j\right) \cdot \Delta t \tag{17}$$

,where $SEDsil$ [t], $SEDarg$ [t] and $SEDsan$ [t] are the load of silt, clay and sand, respectively, leaving the sediment reservoir and reaching the stream network in each time step Δt. The $FRAC$ term (equation 18) corresponds to the fraction of the sediment volume in each reservoir of each HRU .

$$FRAC_{i,j}^t = \frac{VSED_{i,j}^t}{\sum_{j=1}^{N_{URH}} VSED_{i,j}^t} \tag{18}$$

River module

The transport of the suspended loads (silt and clay) in the river network considers an unsteady flow approach, in which the flow velocity and advective processes are dominants. The transport equation, in this case, is given by:

$$\frac{\partial AC}{\partial t} + \frac{\partial AUC}{\partial x} = q_{sm} - q_{sfl} \tag{19}$$

where A [m^2] is the cross-section wetted area; C [t/m^3] is the sediment mean concentration, U [m/s] is the mean flow velocity in the cross-section; x [m] is the distance in the flow direction; t [s] is the time; q_{sm} [t/(m.s)] is the catchment lateral sediment supply; and q_{sfl} [t/(m.s)] is the discharge of sediment exchange between the river and floodplain, considered different of zero only when the hydrodynamic routing is used.

The equation 19 is solved numerically for each suspended particle fraction using a progressive implicit scheme in time and space, which is applied reach to reach, from upstream to downstream:

$$C_i^t = \frac{\theta \cdot Q_{i-1}^t \cdot C_{i-1}^t - (1-\theta)\left(Q_i^{t-1} \cdot C_i^{t-1} - Q_{i-1}^{t-1} \cdot C_{i-1}^{t-1}\right)}{\frac{Vol^t}{\Delta t} + \theta \cdot Q_i^t} + \frac{\frac{Vol^{t-1}}{\Delta t} \cdot C_i^{t-1} + QS_m{}^t - QS_{fl}{}^t}{\frac{Vol^t}{\Delta t} + \theta \cdot Q_i^t} \qquad (20)$$

, where Q [m^3.s-1] is water discharge; the indexes $i-1$ and i refer to the river cross-section upstream and downstream; $t-1$ and t refer to initial and final time step; Δt [s] is calculation time step; θ is the weight of the temporal terms, whose value varies between 0 and 1; $Vol = A \cdot \Delta x$ [m^3] is mean water volume in the river reach; Δx [m] is the length of the catchment river reach; $QS_m = q_{sm} \cdot \Delta x$ [t/s] is sediment load (silt or clay) from the catchment to the river reach; and $QS_{fl} = q_{sfl} \cdot \Delta x$ [t/s] is a sediment load exchange between the river and floodplain.

The cross-section wetted areas (A), related to the respective Q, are calculated using two approaches: (i) for Muskingum-Cunge method, values are calculated for a rectangular channel by multiplication of river width B by water depth h, estimated by Manning equation considering that hydraulic radius Rh is equal h; (ii) in reaches with hydrodynamic flow routing, the h is estimated by the model, and the area A can be directly obtained from Manning equation.

Equations used to represent transport, erosion and deposition of coarse particles (sand) are not presented here, since our study is focused on suspended sediment (silt and clay). For further details the reader is referred to Buarque (2015).

Floodplain module

MGB-SED approach considers that in the floodplains: (i) there are only fine sediments; (ii) sediments are well-mixed and, therefore, concentrations are constant; (iii) longitudinal flow velocity is zero, which allows only lateral exchanges; (iv) floodplains works as fine sediment storage areas. If the net flow of river-plain exchange q_{sfl} [m^3/s] is positive; the water inflow to floodplain will have the same suspended sediment concentration (C) of the river reach. For this case, the solid discharge of river-plain exchange QS_{fl} [t/s] is estimated using equation 21. If q_{sfl} is negative the water outflow from floodplain to the river will have the same suspended sediment concentration of the floodplain (C_{fl} [t/m^3]). For this case, solid discharge QS_{fl} is estimated by equation 22.

$$QS_{fl}{}^{t} = q_{sfl}{}^{t} \cdot \Delta x = q_{fl}{}^{t} \cdot \left(\frac{C_i^t + C_{i-1}^t}{2} \right) \cdot \Delta x \tag{21}$$

$$QS_{fl}{}^{t} = q_{sfl}{}^{t} \cdot \Delta x = q_{fl}{}^{t} \cdot C_{fl}{}^{t} \cdot \Delta x. \tag{22}$$

The sediment concentration in the floodplain is estimated using a time mass balance equation, which is solved numerically for each fraction of particles. For this solution, an implicit scheme progressive in time (equation 23) was used.

$$C_{fl}^{*\,t} = \frac{C_{fl}{}^{t-1} \cdot V_{fl}{}^{t-1} + \left(\frac{q_{fl}{}^{t-1} + q_{fl}{}^{t}}{2} \right) \cdot \Delta x \cdot \Delta t}{V_{fl}{}^{t}} \tag{23}$$

, where V_{fl} [m^3] is the water volume in the floodplain, given by the product between average water depth H_{fl} [m] and flooded area A_{fl} [m^2], estimated by the hydrodynamic model. The percentage of sediments deposited in the floodplain is computed by comparing the H_{fl} with the average vertical distance traveled by each particle in the time step, which is a function of its falling velocity ω_s [m/s]. The volume deposited and the sediment concentration at the end of the time step is estimated using equations 24 and 25, respectively.

$$DEP_{fl}{}^{t} = C_{fl}{}^{t} \cdot V_{fl}{}^{t} \cdot \left(\frac{\omega_s \cdot \Delta t}{H_{fl}} \right) \tag{24}$$

$$C_{fl}{}^{t} = C_{fl}^{*\,t} - \frac{DEP_{fl}{}^{t}}{V_{fl}{}^{t}} \tag{25}$$

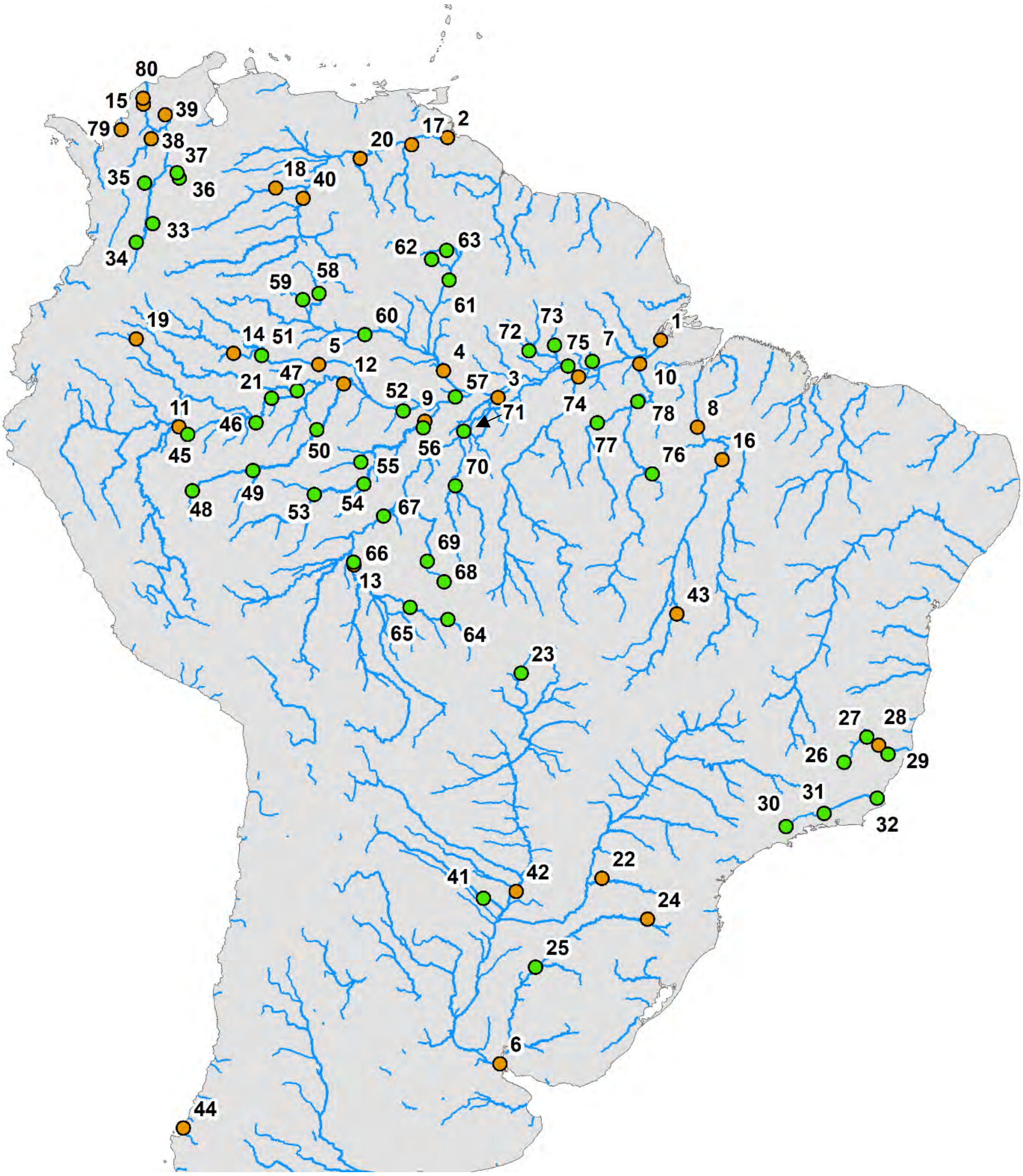

Figure S2. Sites (orange and green) where MGB-SED AS and regional studies data were compared. Numbers are related to ID in Table S1. The Green dots refer to specific sites where comparisons between MGB-SED and WBMsed were made.

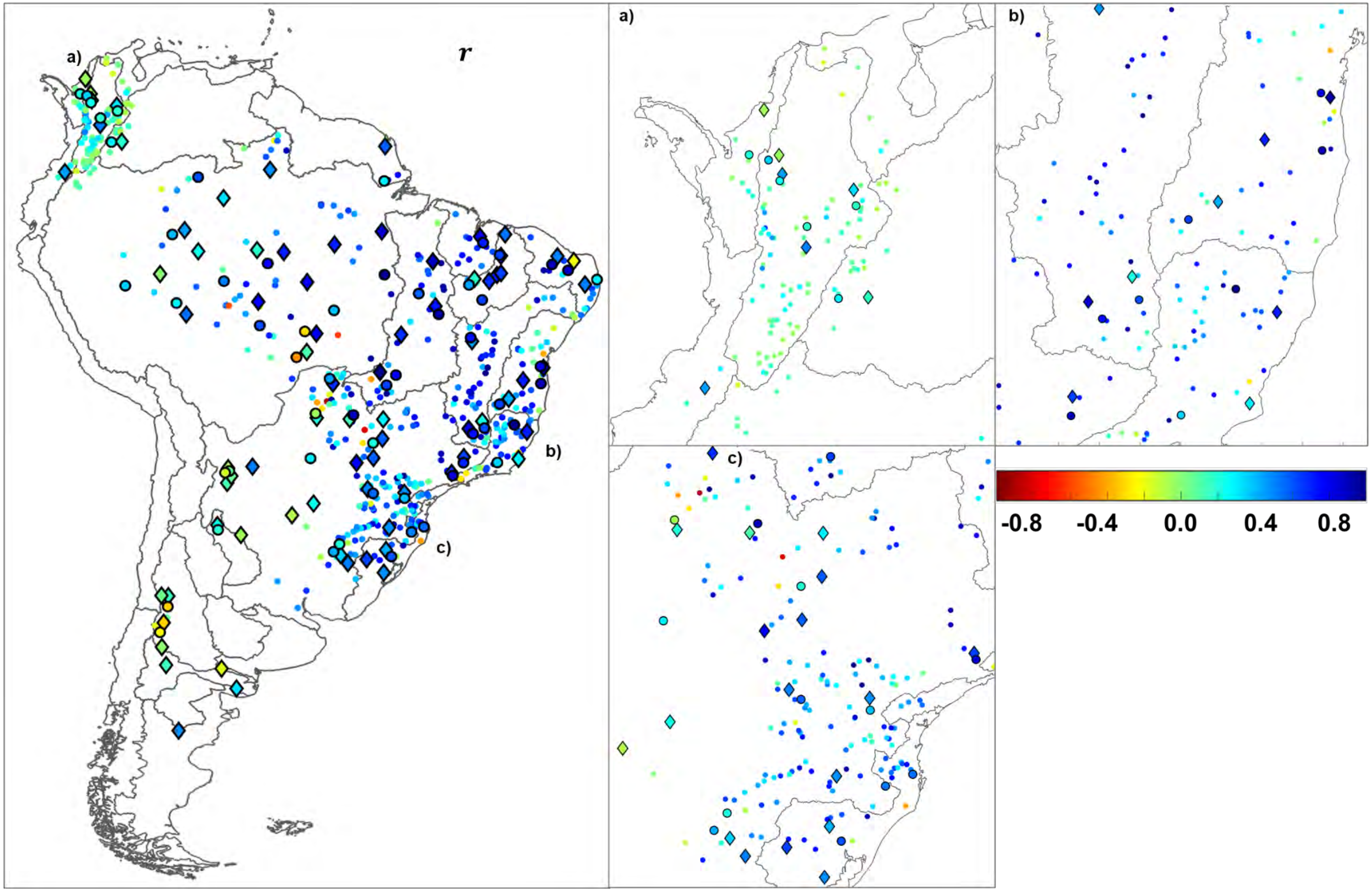

Figure S4: MGB-SED AS performance. Detailed view of Pearson correlation coefficient (r).

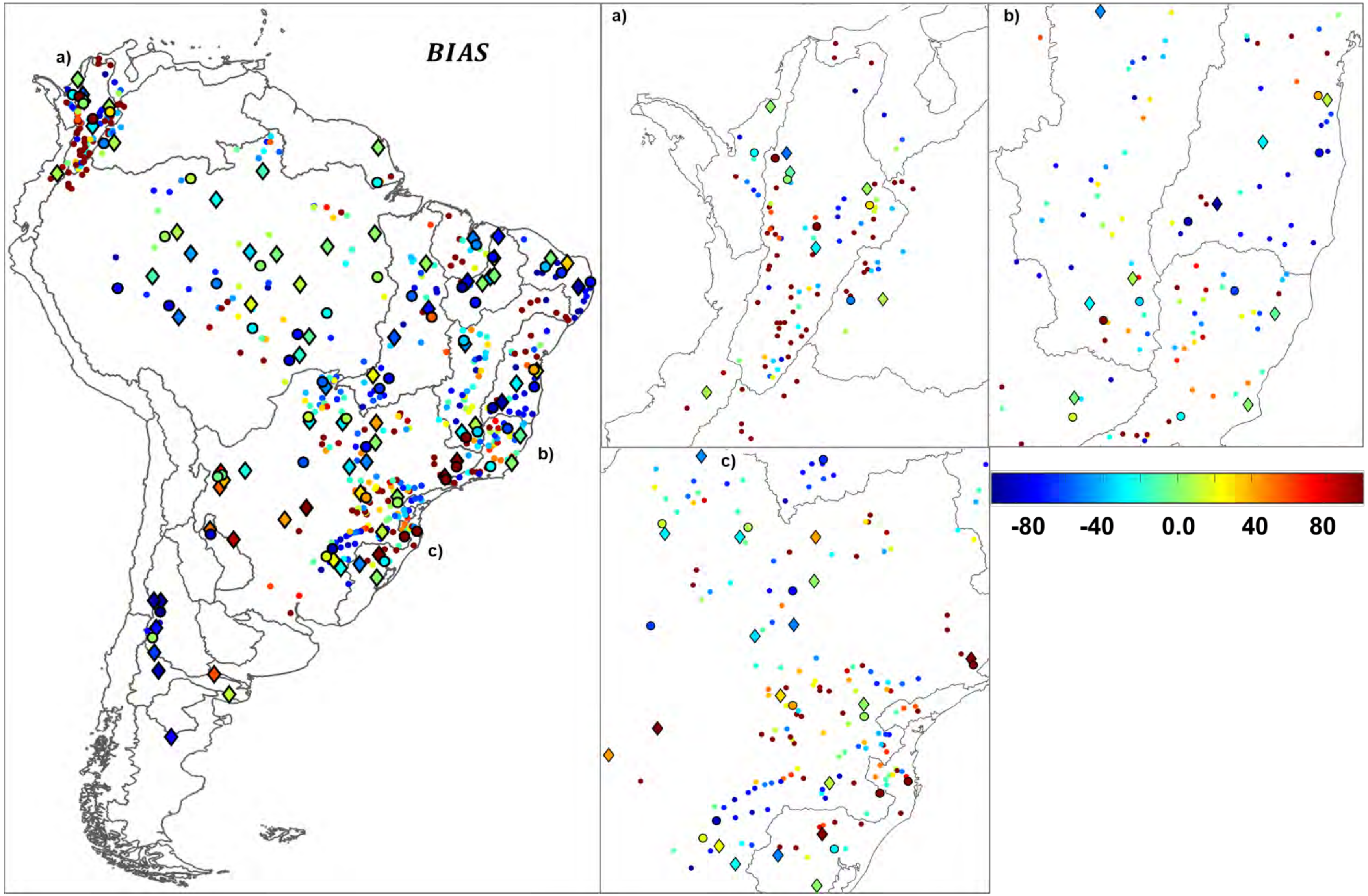

Figure S5: MGB-SED AS performance. Detailed view of $BIAS$.

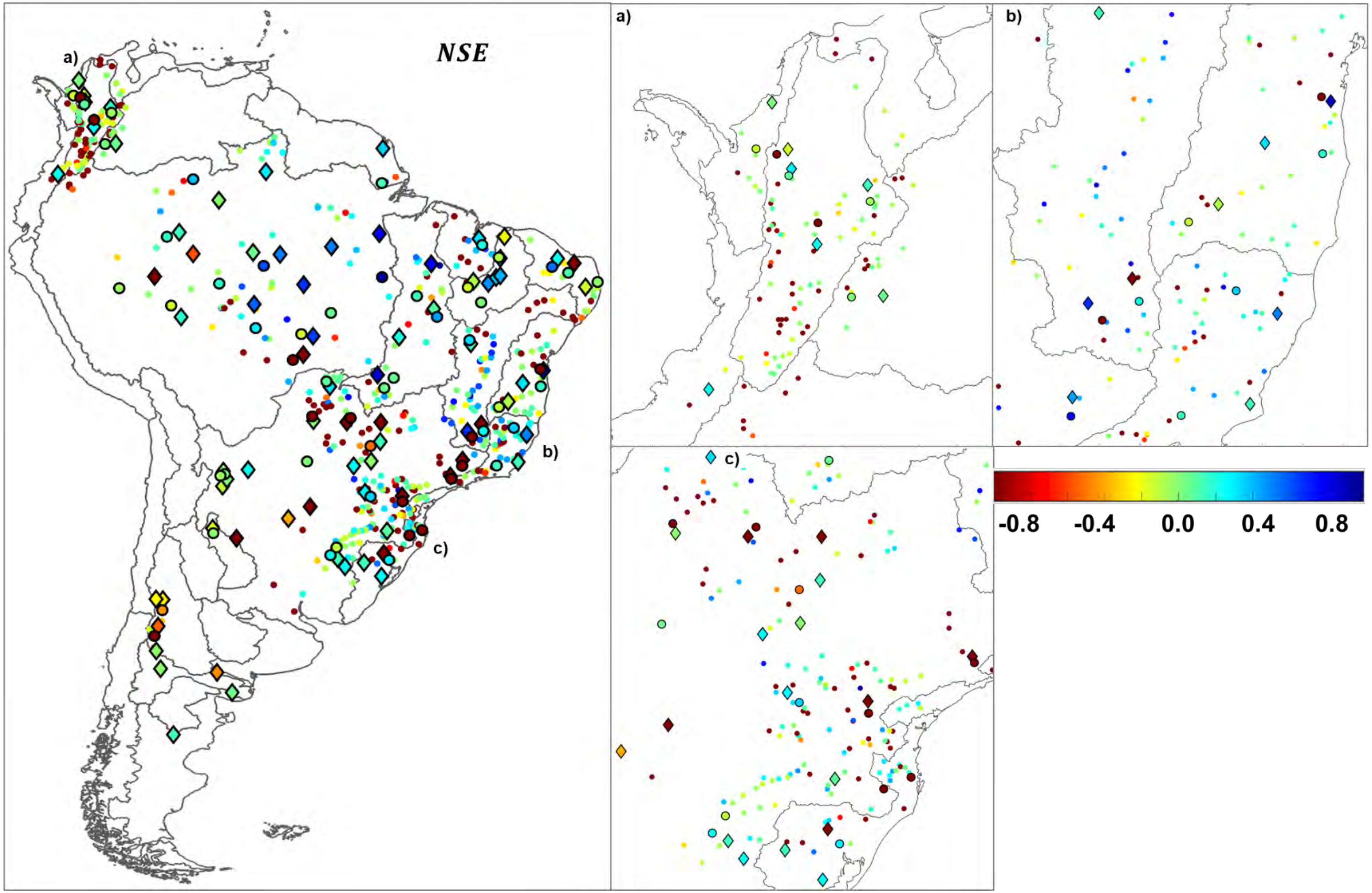

Figure S6: MGB-SED AS performance. Detailed view of NSE.

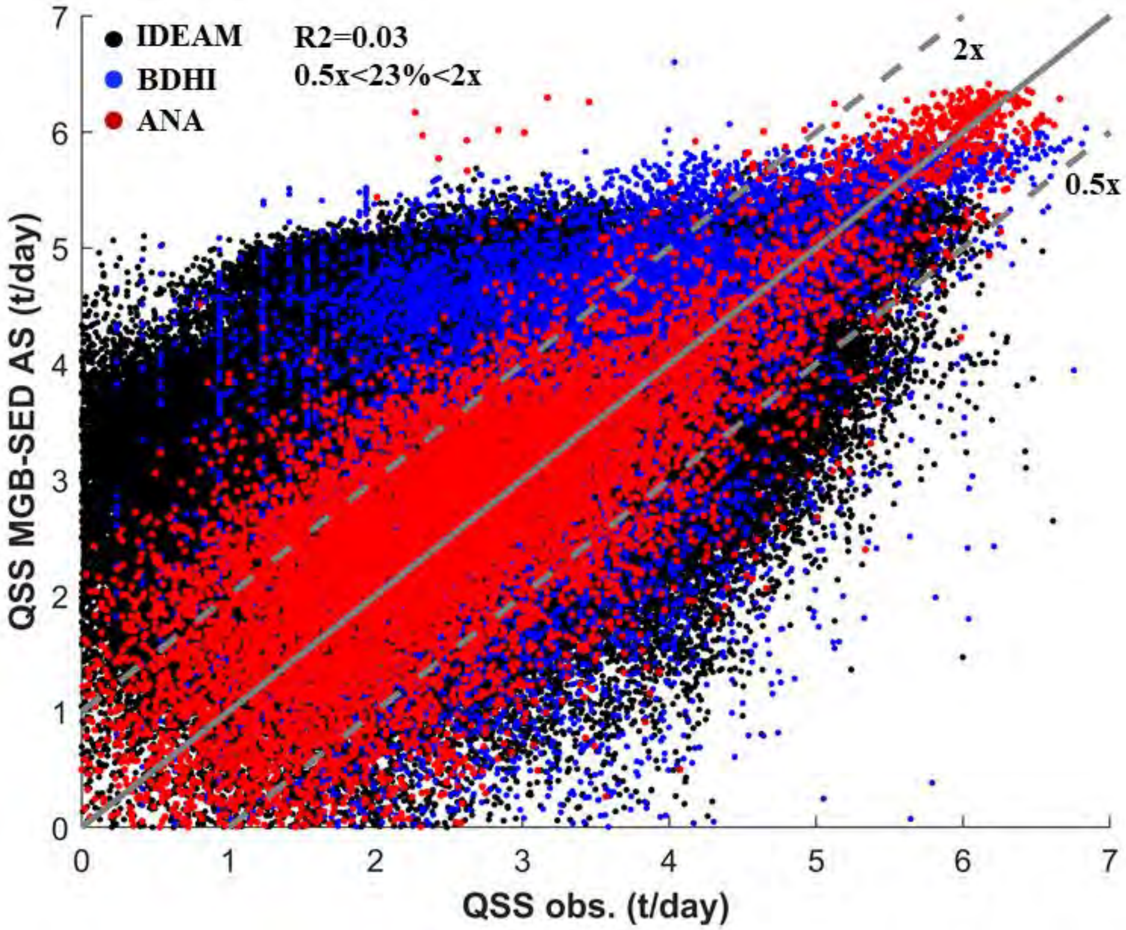

Figure S7: Comparison between all daily observed and simulated QSS.

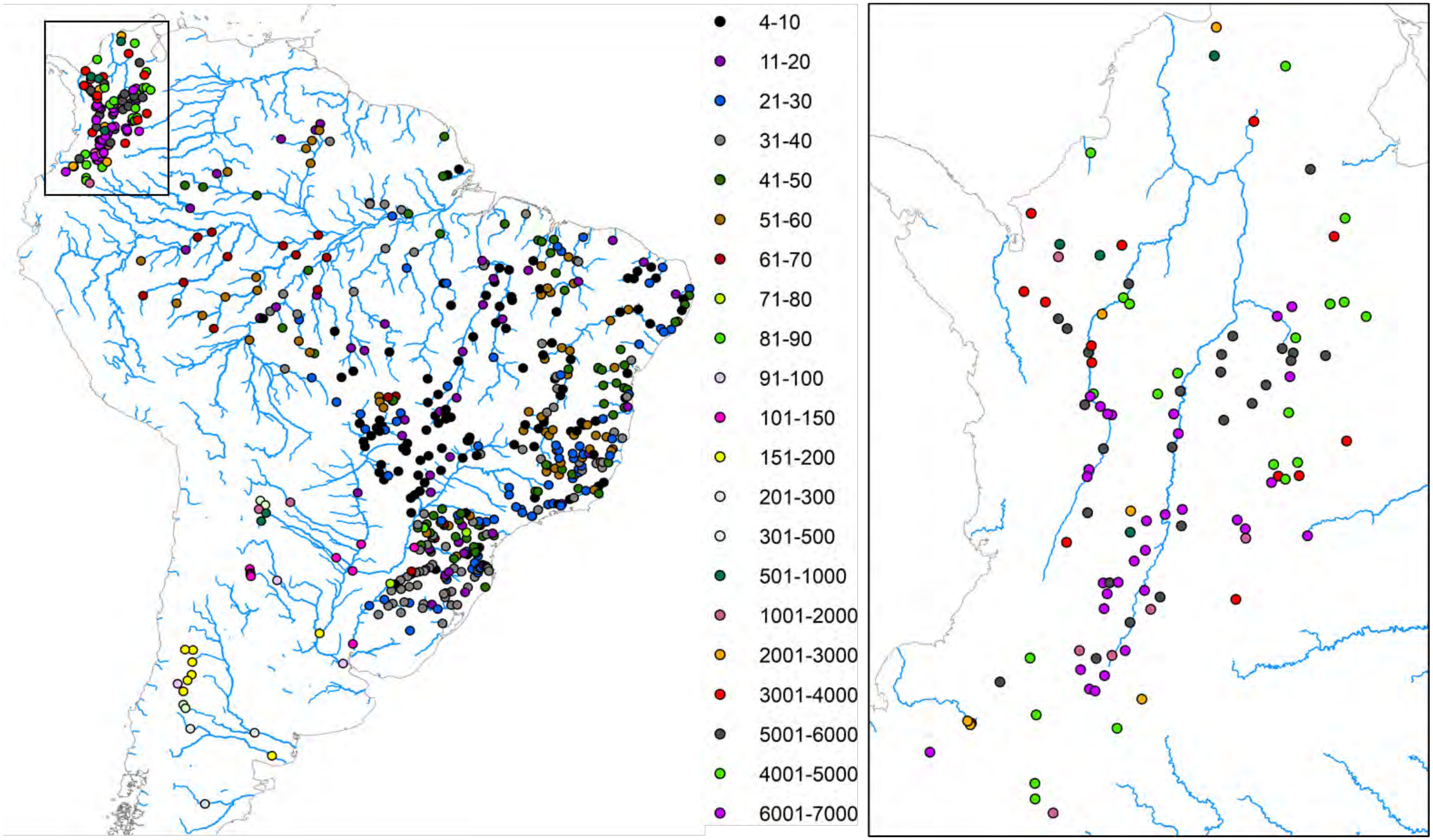

Figure S8: number (n) of discharge of suspended sediment for each station from ANA, IDEAM and BDHI.

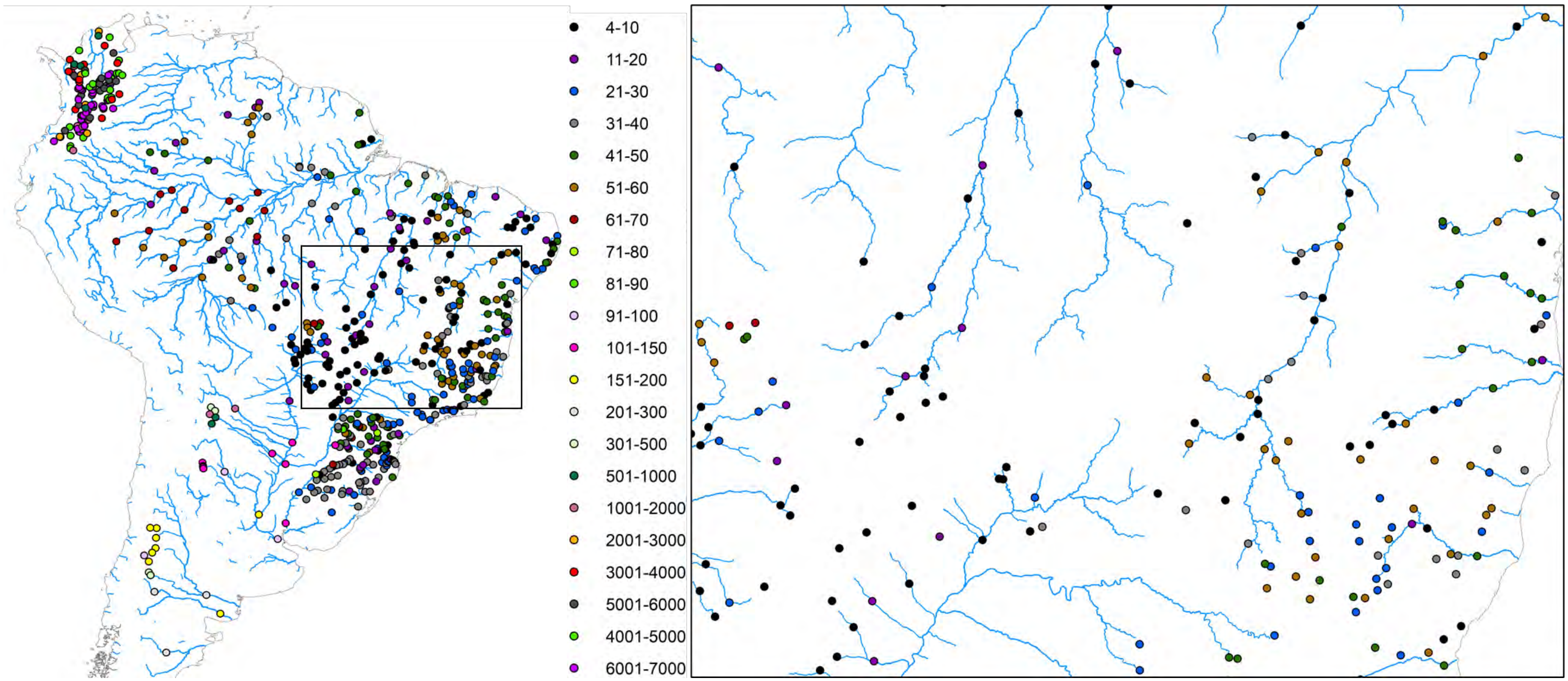

Figure S9: number (n) of discharge of suspended sediment for each station from ANA, IDEAM and BDHI.

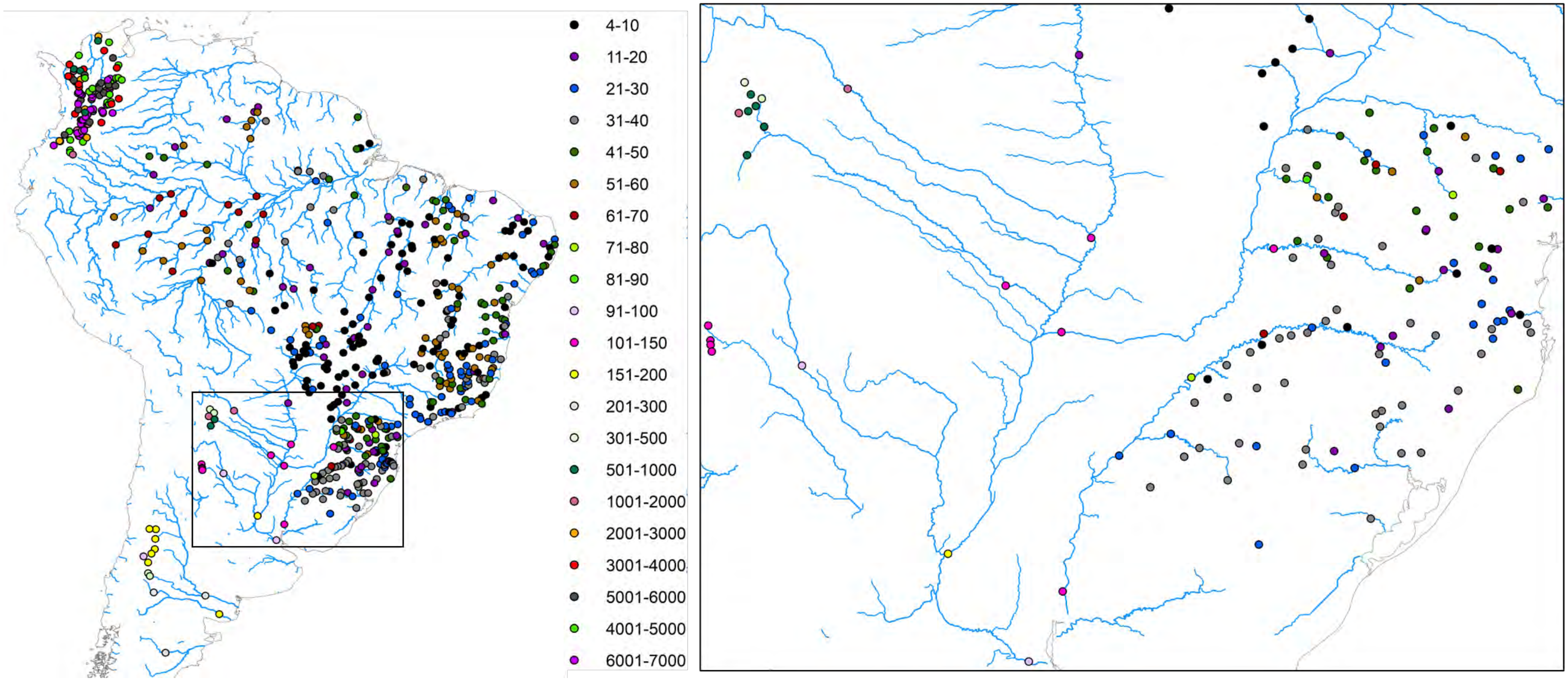

Figure S10: number (n) of discharge of suspended sediment for each station from ANA, IDEAM and BDHI.

Table S1. Summary of water and sediment suspended discharges used to comparison between regional studies and outputs from MGB-SED AS

			Regional Studies				MGB-SED AS				Diff
ID	Source	River	A (km²)	Q (m³/s)	QSS (Mt/year)	QSS (t/year.km²)	A (km²)	Q (m³/s)	QSS (Mt/year)	QSS (t/year.km²)	(%)
1	Filizola[1]	Amazonas	6.00E+06	2.09E+05	1.00E+03	1.67E+02	5.93E+06	2.03E+05	4.37E+02	7.37E+01	-56
2	Meade[2]	Orinoco	9.50E+05	3.50E+04	1.50E+02	1.58E+02	9.41E+05	3.45E+04	1.37E+02	9.46E+01	-9
3	Filizola[1]	Madeira	1.36E+06	3.20E+04	4.50E+02	3.30E+02	1.37E+06	2.91E+04	2.13E+02	1.55E+02	-53
4	Filizola[1]	Negro	6.96E+05	2.84E+04	8.00E+00	1.15E+01	6.99E+05	3.40E+04	7.29E+00	1.04E+01	-9
5	Filizola[1]	Japura	2.48E+05	1.86E+04	3.30E+01	1.33E+02	2.50E+05	1.46E+04	1.86E+01	7.45E+01	-44
6	Amsler[3]	Paraná	2.60E+06	1.80E+04	1.12E+02	4.30E+01	2.60E+06	2.26E+04	1.10E+02	3.95E+01	-2
7	Filizola[1]	Tapajós	4.90E+05	1.35E+04	6.00E+00	1.22E+01	4.95E+05	1.52E+04	3.63E+00	7.33E+00	-39
8	Latrubesse[4]	Tocantins	7.57E+05	1.18E+04	5.80E+01	7.66E+01	7.56E+05	1.32E+04	7.42E+00	9.82E+00	-87
9	Filizola[1]	Purus	3.70E+05	1.10E+04	3.00E+01	8.10E+01	3.72E+05	1.09E+04	1.90E+01	5.11E+01	-37
10	Filizola[1]	Xingu	5.04E+05	9.70E+03	9.00E+00	1.78E+01	5.12E+05	1.37E+04	3.06E+00	5.99E+00	-66
11	Gibs[5]	Ucayali	4.06E+05	9.54E+03	1.25E+02	3.07E+02	3.55E+05	1.03E+04	1.54E+02	4.33E+02	23
12	Filizola[1]	Jurua	1.85E+05	8.44E+03	3.50E+01	1.89E+02	1.82E+05	5.81E+03	2.20E+01	1.21E+02	-37
13	Filizola[1]	Mamore	5.90E+05	8.26E+03	8.00E+01	1.36E+02	5.98E+05	7.08E+03	8.92E+01	1.49E+02	12
14	Nordin[6]	Guaviare	1.14E+05	8.20E+03	3.00E+01	6.78E+02	1.19E+05	7.03E+03	2.86E+01	2.40E+02	-5
15	Milliman[7]	Magdalena	2.57E+05	7.20E+03	1.44E+02	5.45E+02	2.58E+05	7.51E+03	3.32E+01	1.29E+02	-77
16	Latrubesse[4]	Araguaia	3.77E+05	6.10E+03	1.80E+01	4.77E+01	3.77E+05	6.12E+03	2.33E+00	6.18E+00	-87
17	Milliman[7]	Caroni	9.35E+04	5.00E+03	2.00E+00	2.13E+01	9.23E+04	4.18E+03	1.27E+01	3.78E+01	537
18	Milliman[7]	Meta	1.05E+05	4.60E+03	8.00E+01	7.59E+02	1.05E+05	3.98E+03	3.00E+01	2.85E+02	-62
19	Latrubesse[4]	Napo	1.22E+05	4.60E+03	2.24E+01	1.84E+02	1.24E+04	8.58E+02	5.59E+00	4.50E+02	-75
20	Milliman[7]	Caura	4.73E+04	4.00E+03	2.00E+00	4.22E+01	4.75E+04	2.26E+03	1.00E+01	6.11E+01	401
67	Lima[8]	Madeira	9.54E+05	1.93E+04	2.43E+02	2.54E+02	9.82E+05	1.62E+04	2.90E+02	2.96E+02	20
71	Lima[8]	Madeira	1.32E+06	3.06E+04	2.38E+02	1.80E+02	1.32E+06	2.67E+04	2.24E+02	1.70E+02	-6
21	Lima[8]	Solimões	9.91E+05	4.72E+04	3.43E+02	3.46E+02	1.00E+06	4.21E+04	4.00E+02	3.98E+02	17
57	Lima[8]	Solimões	2.15E+06	1.02E+05	4.52E+02	2.11E+02	2.20E+06	9.26E+04	3.55E+02	1.61E+02	-22

74	Lima[8]	Amazonas	4.68E+06	1.81E+05	5.67E+02	1.21E+02	4.70E+06	1.68E+05	4.31E+02	9.17E+01	-24
78	Lima[8]	Xingu	4.46E+05	7.75E+03	3.43E+00	7.70E+00	4.49E+05	1.13E+04	2.59E+00	5.77E+00	-25
22	Lima[8]	Iguaçu	6.32E+04	1.77E+03	2.23E+00	3.53E+01	6.42E+04	1.71E+03	5.15E+00	7.61E+01	131
23	Lima[8]	Paraguai	3.28E+04	5.33E+02	1.26E+00	3.85E+01	3.28E+04	4.88E+02	9.69E-01	3.34E+01	-23
24	Lima[8]	Uruguai	4.13E+04	8.96E+02	1.03E+00	2.49E+01	4.21E+04	1.24E+03	3.03E+00	7.18E+01	194
25	Lima[8]	Uruguai	1.64E+05	4.69E+03	3.59E+00	2.20E+01	1.89E+05	5.49E+03	5.91E+00	3.12E+01	65
26	Lima[8]	Doce	1.01E+04	1.61E+02	1.00E+00	9.96E+01	9.94E+03	1.63E+02	8.52E-01	8.57E+01	-15
27	Lima[8]	Doce	5.54E+04	7.17E+02	6.21E+00	1.12E+02	5.52E+04	7.25E+02	3.51E+00	6.35E+01	-44
28	Lima[8]	Doce	6.16E+04	6.39E+02	6.28E+00	1.02E+02	6.18E+04	7.80E+02	3.86E+00	6.25E+01	-39
29	Lima[8]	Doce	7.58E+04	9.21E+02	1.12E+01	1.48E+02	7.60E+04	9.13E+02	4.68E+00	6.16E+01	-58
30	Lima[8]	Paraíba do Sul	9.58E+03	1.55E+02	2.20E-01	2.25E+01	9.61E+03	1.88E+02	2.88E-01	3.00E+01	31
31	Lima[8]	Paraíba do Sul	1.76E+04	2.73E+02	1.38E+00	7.83E+01	1.81E+04	3.29E+02	5.75E-01	3.18E+01	-58
32	Lima[8]	Paraíba do Sul	5.55E+04	7.91E+02	4.35E+00	7.85E+01	5.62E+04	9.04E+02	2.18E+00	3.87E+01	-50
33	Restrepo[9]	Bogotá	5.54E+03	3.90E+01	1.30E+00	2.39E+02	5.50E+03	5.45E+01	2.28E-01	4.15E+01	-82
34	Restrepo[9]	Saldaña	7.01E+03	3.20E+02	8.90E+00	1.27E+03	6.51E+03	2.44E+02	4.54E+00	6.98E+02	-49
35	Restrepo[9]	Nare	5.71E+03	3.96E+02	2.60E+00	4.52E+02	5.70E+03	2.88E+02	1.32E+00	2.31E+02	-49
36	Restrepo[9]	Suárez	9.31E+03	3.00E+02	3.40E+00	3.67E+02	1.02E+04	2.90E+02	1.81E+00	1.77E+02	-47
37	Restrepo[9]	Sogamo	2.15E+04	4.88E+02	1.12E+01	5.22E+02	2.13E+04	4.89E+02	5.20E+00	2.43E+02	-54
38	Restrepo[9]	Cauca	5.96E+04	2.37E+03	4.91E+01	8.23E+02	5.96E+04	2.39E+03	2.00E+01	3.36E+02	-59
39	Restrepo[9]	Cesar	1.67E+04	5.30E+01	2.00E-01	1.00E+01	1.69E+04	2.02E+02	1.30E+00	7.66E+01	549
40	Meade[2]	Orinoco	-	1.57E+04	3.20E+01	-	3.42E+05	1.66E+04	4.15E+01	5.32E+01	30
41	Alarcon[10]	Bermejo	-	-	1.09E+02	-	1.06E+05	5.10E+02	2.56E+01	3.08E+02	-77
42	Alarcon[10]	Paraguay	-	-	5.20E+00	-	9.72E+05	3.88E+03	3.09E+01	3.89E+01	495
43	Carvalho[11]	Araguaia	-	3.64E+03	5.53E+00	-	1.18E+05	1.73E+03	1.33E+00	1.13E+01	-76
44	Aros[12]	Bio Bio	2.43E+04	1.00E+03	5.94E+00	2.45E+02	2.44E+04	1.08E+03	4.18E+01	1.52E+03	603
45	Filizola[13]	Javari	1.20E+04	6.40E+02	1.34E+00	1.12E+02	1.68E+04	5.65E+02	1.01E-01	6.01E+00	-92
46	Filizola[13]	Solimões	9.83E+05	4.42E+04	4.35E+02	4.42E+02	9.95E+05	4.16E+04	4.01E+02	4.03E+02	-8
47	Filizola[13]	Solimões	1.14E+06	5.49E+04	4.73E+02	4.17E+02	1.14E+06	5.04E+04	4.14E+02	3.62E+02	-13

48	Filizola[13]	Juruá	3.90E+04	9.10E+02	1.23E+01	3.15E+02	3.82E+04	9.48E+02	5.35E+00	1.40E+02	-56
49	Filizola[13]	Juruá	7.70E+04	1.78E+03	1.18E+01	1.53E+02	7.73E+04	2.21E+03	8.42E+00	1.09E+02	-29
50	Filizola[13]	Juruá	1.62E+05	4.75E+03	2.55E+01	1.57E+02	1.65E+05	5.05E+03	2.25E+01	1.36E+02	-12
51	Filizola[13]	Japurá	1.97E+05	1.37E+04	2.64E+01	1.34E+02	2.08E+05	1.24E+04	3.00E+01	1.44E+02	14
52	Filizola[13]	Solimões	1.77E+06	8.40E+04	5.10E+02	2.88E+02	1.79E+06	7.99E+04	4.46E+02	2.50E+02	-13
53	Filizola[13]	Purus	1.53E+05	3.65E+03	1.03E+02	6.71E+02	1.54E+05	3.84E+03	1.51E+01	9.78E+01	-85
54	Filizola[13]	Purus	2.20E+05	5.52E+03	6.84E+01	3.11E+02	2.28E+05	6.00E+03	1.84E+01	8.07E+01	-73
55	Filizola[13]	Cuniua	3.80E+04	1.49E+03	7.44E+00	1.96E+02	3.84E+04	1.26E+03	1.29E+00	3.37E+01	-83
56	Filizola[13]	Purus	3.60E+05	1.07E+04	2.47E+01	6.85E+01	3.69E+05	1.07E+04	1.90E+01	5.16E+01	-23
57	Filizola[13]	Solimões	2.15E+06	9.88E+04	4.03E+02	1.88E+02	2.20E+06	9.26E+04	3.55E+02	1.61E+02	-12
58	Filizola[13]	Negro	6.20E+04	4.84E+03	9.70E-01	1.56E+01	7.43E+04	4.23E+03	1.04E+00	1.41E+01	8
59	Filizola[13]	Içana	2.20E+04	1.88E+03	2.70E-01	1.23E+01	2.37E+04	1.67E+03	1.47E-01	6.20E+00	-45
60	Filizola[13]	Negro	2.80E+05	1.61E+04	3.89E+00	1.39E+01	2.98E+05	1.81E+04	2.85E+00	9.58E+00	-27
61	Filizola[13]	Uraricoera	3.80E+04	1.02E+03	1.00E+00	2.63E+01	3.67E+04	1.15E+03	1.13E+00	3.08E+01	13
62	Filizola[13]	Mucajai	1.40E+04	2.80E+02	3.40E-01	2.43E+01	1.21E+04	3.46E+02	2.73E-01	2.26E+01	-20
63	Filizola[13]	Branco	1.25E+05	2.90E+03	2.74E+00	2.19E+01	1.26E+05	3.62E+03	3.46E+00	2.75E+01	26
64	Filizola[13]	Guaporé	3.00E+03	6.00E+01	2.40E-01	8.00E+01	5.48E+04	5.19E+02	8.50E-01	1.55E+01	254
65	Filizola[13]	Guaporé	1.10E+05	9.10E+02	1.40E-01	1.27E+00	1.10E+05	1.17E+03	1.14E+00	1.04E+01	717
66	Filizola[13]	Mamoré	5.89E+05	8.40E+03	5.65E+01	9.58E+01	6.15E+05	7.45E+03	8.93E+01	1.45E+02	58
67	Filizola[13]	Madeira	9.54E+05	1.94E+04	2.77E+02	2.91E+02	9.82E+05	1.62E+04	2.90E+02	2.96E+02	5
68	Filizola[13]	Pimenta Bueno	1.20E+04	2.10E+02	1.30E-01	1.08E+01	1.01E+04	2.22E+02	2.03E-01	2.01E+01	56
69	Filizola[13]	Jiparana	3.30E+04	7.20E+02	1.53E+00	4.64E+01	3.33E+04	7.54E+02	4.73E-01	1.42E+01	-69
70	Filizola[13]	Aripuanã	1.09E+05	3.38E+03	2.57E+00	2.36E+01	1.31E+05	3.68E+03	8.46E-01	6.44E+00	-67
71	Filizola[13]	Madeira	1.33E+06	3.13E+04	2.44E+02	1.84E+02	1.32E+06	2.67E+04	2.24E+02	1.70E+02	-8
72	Filizola[13]	Mapuera	2.60E+04	7.30E+02	6.00E-01	2.31E+01	2.58E+04	5.91E+02	4.70E-01	1.82E+01	-22
73	Filizola[13]	Erepecuru	3.50E+04	5.20E+02	1.80E-01	5.14E+00	3.48E+04	7.30E+02	3.54E-01	1.02E+01	97
74	Filizola[13]	Amazonas	4.62E+06	1.69E+05	5.56E+02	1.20E+02	4.70E+06	1.68E+05	4.31E+02	9.17E+01	-22
75	Filizola[13]	Maicuru	1.30E+04	1.20E+02	1.20E-01	9.23E+00	1.26E+04	2.12E+02	1.78E-01	1.42E+01	48

76	Filizola[13]	Fresco	4.20E+04	8.30E+02	1.37E+00	3.26E+01	4.25E+04	1.04E+03	6.25E-01	1.47E+01	-54
77	Filizola[13]	Iriri	1.24E+05	2.69E+03	2.56E+00	2.06E+01	1.23E+05	3.79E+03	6.23E-01	5.07E+00	-76
78	Filizola[13]	Xingu	4.46E+05	8.72E+03	5.80E+00	1.30E+01	4.49E+05	1.13E+04	2.59E+00	5.77E+00	-55
79	López[14]	Sinú	1.47E+04	-	3.02E+00	2.05E+02	9.84E+03	5.60E+02	1.76E+00	1.79E+02	-42
80	López[14]	Magdalena	2.57E+05	-	1.41E+02	5.47E+02	2.59E+05	7.51E+03	3.30E+01	1.27E+02	-77

[1] Filizola, N.P., 1999. O fluxo de sedimentos em suspensão nos rios da bacia Amazônica Brasileira. ANEEL, Brasília (63 pp.).

[2] Meade, R. H., Weibezahn, F. H., Lewis Jr, W. M.; Hernandez, D. P., 1990. Suspended-sediment budget for the Orinoco River. The Orinoco River as an ecosystem, 55-79.

[3] Amsler, M., Prendes, H., 2000. Transporte de sedimentos y processos fluviales asociados. In: Paoli, C., Schreider, M. (Eds.), El Río Paraná en su Tramo Medio. Centro de Publicaciones Universidad Nacional del Litoral, Santa Fé, Argentina, pp. 233–306.

[4] Latrubesse, E.M., Stevaux, J.C., Sinha, R., 2005. Tropical rivers. Geomorphology 70, 187–206.

[5] Gibss, R., 1967. The geochemistry of the Amazon river system: Part 1. The factors that control the salinity and the co position and concentration of the suspended solids. Geological Society of America Bulletin 78, 1203– 1232.

[6] Nordin, C.F., Mejia, A., Delgado, C., 1994. Sediment studies of the Orinoco river, Venezuela. In: Schumm, S., Winkley, B. (Eds.), The Variability of Large Alluvial Rivers. ASCE Press, pp. 243–265.

[7] Milliman, J.D., Farnsworth, K.L., Albertin, Ch., 1999. Flux and fate of fluvial sediments leaving large islands in the East Indies. Journal of Sea Research 41, 97–107.

[8] Lima, J.E.F.W., Lopes, W.T.A., Carvalho, N. O., Vieira, M.R., Da Silva, E.M., 2005. Suspended sediment fluxes in the large river basins of Brazil. IAHS ICCE Symp. Sediments Budgets 1 1, 355–364.

[9] Restrepo, J.D., Kjerfve, B., Hermelin, M., Restrepo, J.C., 2006. Factors controlling sediment yield in a major South American drainage basin: The Magdalena River, Colombia. J. Hydrol. 316, 213–232.

[10] Alarcón, J. J., Szupiany, R., Montagnini, M. D., Gaudin, H., Prendes, H. H., Amsler, M. L., 2003. Evaluación del transporte de sedimentos en el tramo medio del río Paraná. In Primer Simposio Regional sobre Hidráulica de Ríos. Argentina: Ezeiza.

[11] Carvalho, T. M., 2009. Avaliação do transporte de carga sedimentar no médio rio Araguaia. Geosul, 24(47), 147-160.

[12] Araya, V. A., 1990. Análisis sedimentológico del río Bío Bío Bajo. Parte I. – Rev. Soc. Chil. Ingen. Hidraul. 5(2): 21-40.

[13] Filizola, N., Guyot, J. L., 2009. Suspended sediment yields in the Amazon basin: an assessment using the Brazilian national data set. Hydrological Processes: An International Journal, 23(22), 3207-3215.

[14] López, J. C. R., Torregroza, A. C., 2017. Suspended sediment load in northwestern South America (Colombia): A new view on variability and fluxes into the Caribbean Sea. Journal of South American Earth Sciences, 80, 340-352.

Table S2. Summary of water and sediment suspended discharge used to the comparison between regional studies and outputs from MGB-SED AS

		WBM-SED[1]	MGB-SED AS	*Diff (%)*	*Daily BIAS (%)*
ID	**River**	**QSS (Mt/year)**	**QSS (Mt/year)**		
67	Madeira	2.43E+02	2.90E+02	-44	-52
71	Madeira	2.38E+02	2.24E+02	-71	-3
21	Solimões	3.43E+02	4.00E+02	-35	5
57	Solimões	4.52E+02	3.55E+02	-76	8
74	Amazonas	5.67E+02	4.31E+02	-83	32
78	Xingu	3.43E+00	2.59E+00	-96	0
23	Paraguai	1.26E+00	9.69E-01	-74	-40
25	Uruguai	3.59E+00	5.91E+00	-73	-7
26	Doce	1.00E+00	8.52E-01	-32	-11
27	Doce	6.21E+00	3.51E+00	-40	-65
29	Doce	1.12E+01	4.68E+00	-45	-8
30	Paraíba do Sul	2.20E-01	2.88E-01	-74	14
31	Paraíba do Sul	1.38E+00	5.75E-01	-81	23
32	Paraíba do Sul	4.35E+00	2.18E+00	-77	1
33	Bogotá	1.30E+00	2.28E-01	-92	-43
34	Saldaña	8.90E+00	4.54E+00	-25	132
35	Nare	2.60E+00	1.32E+00	-21	60
36	Suárez	3.40E+00	1.81E+00	-70	30
37	Sogamo	1.12E+01	5.20E+00	-71	6
41	Bermejo	1.09E+02	2.56E+01	5	42
45	Javari	1.34E+00	1.01E-01	-94	-95
46	Solimões	4.35E+02	4.01E+02	-34	2
47	Solimões	4.73E+02	4.14E+02	-43	8
48	Juruá	1.23E+01	5.35E+00	92	-72
49	Juruá	1.18E+01	8.42E+00	7	-12
50	Juruá	2.55E+01	2.25E+01	58	-44
51	Japurá	2.64E+01	3.00E+01	-82	0
52	Solimões	5.10E+02	4.46E+02	-63	29
53	Purus	1.03E+02	1.51E+01	19	-69
54	Purus	6.84E+01	1.84E+01	14	-47
55	Cuniua	7.44E+00	1.29E+00	31	72
56	Purus	2.47E+01	1.90E+01	-33	-10
58	Negro	9.70E-01	1.04E+00	-97	10
59	Içana	2.70E-01	1.47E-01	-94	-47
60	Negro	3.89E+00	2.85E+00	-97	-25
61	Uraricoera	1.00E+00	1.13E+00	-90	-18
62	Mucajai	3.40E-01	2.73E-01	-90	-49
63	Branco	2.74E+00	3.46E+00	-90	-1
64	Guaporé	2.40E-01	8.50E-01	-84	173
65	Guaporé	1.40E-01	1.14E+00	-90	304
66	Mamoré	5.65E+01	8.93E+01	-71	91
68	Pimenta Bueno	1.30E-01	2.03E-01	-77	-7
69	Jiparana	1.53E+00	4.73E-01	-87	-29
70	Aripuanã	2.57E+00	8.46E-01	-94	-65
72	Mapuera	6.00E-01	4.70E-01	-91	-5
73	Erepecuru	1.80E-01	3.54E-01	-92	66
75	Maicuru	1.20E-01	1.78E-01	-94	-8
76	Fresco	1.37E+00	6.25E-01	-87	21
77	Iriri	2.56E+00	6.23E-01	-95	-17

[1] Cohen, S., Kettner, A.J., Syvitski, J.P.M., 2014. Global suspended sediment and water discharge dynamics between 1960 and 2010: Continental trends and intra-basin sensitivity. Glob. Planet. Change 115, 44–58.

Table S3. QSS (Mt/year) for the main South America rivers. Bold values refers to rivers reaching the Ocean.

River	QSS (Mt/year)
Amazon	**436.83**
Madeira	213.40
Marañon	202.12
Ucayali	153.68
Orinoco	**136.97**
Prata	**111.76**
Beni	110.32
Madre de Dios	91.11
Mamoré Grande	84.59
Magdalena	**32.59**
Pilcomayo	25.66
Grande	25.58
Bermejo	24.36
Juruá	22.03
Purus	18.75
Tietê	16.94
Paranaíba	15.68
São Francisco	**7.46**
Tocantins	**7.44**
Negro (Amazon)	7.25
Uruguai	**5.88**
Paraná-Panema	5.53
Iguaçu	5.27
Doce	**5.04**
Guaporé	4.72
Jacuí	**3.70**
Tapajós	3.63
Xingu	3.04
Araguaia	2.44
Paraíba do Sul	**2.15**
Parnaíba	**1.23**
Negro	**0.64**
Salado	**0.55**
Jequitinhonha	**0.54**
Colorado	0.37
Desaguadero Salado	**0.07**

Table S4. Sediment balance for the whole South America and simulation time (1990-2009)

	Input	Deposition	Storage in river reaches	Output	Error (%)
Silt	1.54E+12	1.89E+09	5.16E+07	1.54E+12	5.62E-02
Clay	3.32E+12	2.11E+09	1.53E+08	3.32E+12	2.59E-02

Table S5. Performance analysis for MGB-SED AS for calibration (2002-2009) and non-calibration period (1992-2001), considering temporal and spatial extrapolations. #1 refers to calibration step with selected stations. #2 refers to temporal extrapolation with selected stations of #1 with available data in interval of #2. #3 refer to spatial extrapolation considering selected station of validation step in calibration period. #4 refer to all simulation period with calibration stations. #5, #6 and #7 represent spatial, spatial and temporal and global assessments of MGB-SED AS performance. Many stations do not have data in all simulation period. Results were summarized using median values.

#	Interval	*r*	*NSE*	*BIAS*	Notes
1	2002-2009	0.54	0.02	-11.79	Calib. (77 stations)
2	1992-2001	0.51	0.01	-10.47	Temporal extrap. (65 stations)
3	2002-2009	0.65	-0.03	-35.90	Spatial extrap. (47 stations)
4	1992-2009	0.54	0.08	-2.89	All simulation period (77 stations)
5	2002-2009	0.57	-0.13	-0.04	Spatial extrap. (515 stations)
6	1992-2001	0.49	-0.07	-0.06	Spatial and temporal extrap. (488 stations)
7	1992-2009	0.50	-0.05	-0.76	All simulation period (595 stations)